

Photocopy and Use Authorization

In presenting this thesis in partial fulfillment of the requirements for an advanced degree at Idaho State University, I agree that the Library shall make it freely available for inspection. I further state that permission to download, print my thesis for scholarly purposes may be granted by the Dean of the Graduate School, Dean of my academic division, or by the University Librarian. It is understood that any copying or publication of this thesis for financial gain shall not be allowed without my written permission.

Signature _____

Date _____

Using experiments designed to provide data to Validate
High-Fidelity and Systems Analysis Numerical Models to
enhance understanding of Integral System Experiment
Behavior and the Adequacy of Analysis Tools

by

Maruf Anwarul

A thesis

submitted in partial fulfillment

of the requirement for the degree of

Master of Science in the Department of Nuclear Science and Engineering

Idaho State University

Spring 2018

To the Graduate Faculty:

The members of the committee appointed to examine the thesis of Maruf Anwarul find it satisfactory and recommend that it be accepted.

Dr. Richard R. Schultz

Major Advisor

Dr. Jay F. Kunze

Committee Member

Dr. Ken W. Bosworth

Graduate Faculty Representative

Acknowledgments

I would like to thank my advisor, Dr. Richard R. Schultz for his guidance and support throughout my research. Courses such as Validation & Verification; Thermal Hydraulics; and CFD instructed by him at ISU; helped me immensely in furnishing this report. He has always been there for me to provide scholarly materials and sound advice whenever I needed. Special thanks goes to Dr. Jay F. Kunze, who helped me to change my major from mechanical engineering to nuclear engineering. I am grateful to Dr. Hans Gougar, Director, INL ART TDO, for arranging financial assistance through INL. Also, my Mom, without her encouragement I would not be able to pursue Masters degree in nuclear engineering.

Table of Contents

List of Figures	vii
List of Tables	ix
Abbreviations	x
Nomenclature	xi
Non-Dimensional Ratios.....	xii
Greek Symbols.....	xiii
Subscripts, Superscripts, and Other Symbols	xiv
Abstract.....	xv
1. Introduction.....	1
1.1 Goal of this research.....	6
2. Objectives and Approach.....	6
3. Description of the Experimental Facilities	7
3.1 Modular High Temperature Gas Reactor (MHTGR).....	7
3.2 High Temperature Test Facility (HTTF) at OSU.....	9
3.3 City College of New York (CCNY) Test Facility.....	10
3.4 Texas A&M University (TAMU) Upper Plenum Mixing Test Facility	10
3.5 Matched Index of Refraction (MIR) Facility at INL.....	11
4. Hierarchical 2-Tiered Scaling (H2TS) Analysis Method	13
5. Pressurized Conduction Cooldown Events.....	18
5.1 Flow distribution and heat transfer.....	19
5.2 Upper plenum jet impingement.....	20
6. Normal Operational Condition Events.....	21
6.1 Coolant, bypass flow, and temperature distribution.....	21

6.2 Lower plenum mixing and jet impingement	22
7. Scaling Analysis of Pressurized Conduction Cooldown Event	24
7.1 Single Phase Natural Circulation	24
7.1.1 Single-Phase Natural Circulation Loop Scaling Analysis	25
7.1.2 Primary Loop Resistance.....	30
7.1.3 Heat Transfer	31
7.2 Upper Plenum Mixing and Heat Transfer.....	34
8. Scaling Analysis of Single Phase Forced Convection	40
8.1 Normal Operations Loop Scaling Analysis.....	40
8.2 Heat Transfer.....	40
8.3 Lower Plenum Mixing	42
9. Distortion Analysis	46
9.1 Pressurized Conduction Cooldown Event Scaling Evaluation	46
9.1.1 Natural Circulation	46
9.1.2 PCC Upper Plenum Mixing and Heat Transfer.....	51
9.2 Single Phase Forced Convection Scaling Evaluation	52
9.2.1 Normal Operations	52
9.2.2 Outlet Plenum Mixing	53
10. Using Vintage Data to Validate Modern Numerical Methods: Data Superposition.....	54
10.1 Conceptual Approach.....	54
10.1.1 Background.....	56
10.1.2 Issue	56
10.2 Projected Reynolds Number and Gas Temperatures in VHTR Upper Plenum: PCC and DCC Scenarios	57

10.2.1 PCC Scenario.....	57
10.2.2 DCC Scenario.....	58
10.2.3 Concluding Remarks on Data Superposition.....	59
11. Previously Conducted Experiments.....	62
11.1 Heated vertical tube ("hot channel" issue).....	62
11.2 Lower plenum ("hot streaking" issue).....	69
11.3 Lower plenum mixing.....	70
12. Summary.....	72
13. References.....	74

List of Figures

Figure 1: Typical Validation Pyramid	4
Figure 2: MHTGR Module (DOE 1986)	7
Figure 3: Plan view of reactor vessel and internals in an elevation through the core region (DOE 1986)	8
Figure 4: Oregon State University High Temperature Test Facility.....	9
Figure 5: Schematic Diagram of City College of New York (CCNY) Core Heat Transfer Facility	10
Figure 6: Upper Plenum Mixing Test Facility at TAMU	11
Figure 7: Schematic diagram of temperature control system for typical internal flow experiment in INL MIR flow system.....	12
Figure 8: General Approach for System Breakdown in the H2TS Methodology.....	13
Figure 9: Single-Phase Natural Circulation	18
Figure 10: Intracore Natural Circulation.....	19
Figure 11: Axisymmetric Impinging Jet.....	20
Figure 12: Normal Operational Condition.....	21
Figure 13: Relation of "hot channel" and "hot streaking" issues	23
Figure 14: Scaling Analysis Flow Diagram for Single Phase Natural Circulation (PCC)	24
Figure 15: Jet mixing in Upper Plenum.....	34
Figure 16: MHTGR Outlet Plenum	43
Figure 17: Average Reynolds Number of gases moving from core into upper plenum	59
Figure 18: Average temperature of gases moving from core into upper plenum of MHTGR during PCC scenario from rings 1, 2, and 3.....	60
Figure 19: Average Reynolds Number of gases moving from core into upper plenum of MHTGR during DCC scenario from rings 1, 2, and 3	60

Figure 20: Average Reynolds Number of gases moving from core into upper plenum of MHTGR during DCC scenario from rings 1, 2, and 3	61
Figure 21: Effects of buoyancy on convective heat transfer for fully-developed flow in vertical circular tubes [Jackson, Cotton and Axcell, 1989; Li, 1994].....	63
Figure 22: Prediction of local heat transfer parameters for air and helium in laminar flow, accounting for effects of gas property variation [Worsoe-Schmidt, IJHMT 1966].....	64
Figure 23: Effects of buoyancy on heated, fully-established laminar flow in vertical circular tubes with the Boussinesq approximation [Scheelee and Hanratty, JFM 1962].....	65
Figure 24: Operating conditions maps for NGNP Point Design during normal full and reduced power operations, order-of-magnitude estimates: a) non-dimensional heat flux (indicator of significance of property variation, b) acceleration parameter and c) buoyancy para	66
Figure 25: Low-Reynolds-number predictions for fully-established flow in a circular tube with constant properties from various turbulence models [Mikielewicz et al., 2002], normalized by Dittus-Boelter correlation [1930]. Curve labeled P-K is an accepted empirica	67
Figure 26: Preliminary assessment of turbulence models via wall temperature data of Shehata [Shehata and McEligot, 1998; Richards, Spall and McEligot, 2004].....	68
Figure 27: Conditions for which tabulated internal gas heat transfer (and some friction) data are available.	68
Figure 28: CFD predictions of flow paths and temperatures in a computer model of the lower plenum of a MHTGR (courtesy of General Atomics Co).....	69
Figure 29: Examples of some possible flow paths in the lower plenum of a typical NGNP concept.	70
Figure 30: Schematic diagram of conceptual design of MIR experiment model to study mixing, turbulence and flow fields in the lower plenum of an NGNP.....	71

List of Tables

Table 1: Effects of buoyancy on convective heat transfer	49
Table 2: Characteristic ratios and Flow parameters for PCC natural circulation upper plenum jet impingement (TAMU, MHTGR).....	50
Table 3: Characteristic ratios for PCC Upper plenum mixing (TAMU, MHTGR).....	51
Table 4: Characteristic ratios for PCC natural circulation heat transfer (CCNY, HTTF)	51
Table 5: Characteristic ratios for normal operations.....	53

Abbreviations

CCNY	City College of New York
CFD	Computational Fluid Dynamics
DOE	US Department of Energy
H2TS	Hierarchal Two-Tiered Scaling Methodology
HTGR	High Temperature Gas Reactor
HTTF	High Temperature Test Facility
INL	Idaho National Lab
LOFC	Loss of Forced Convection
MIR	Matched Index of Refraction
MHTGR	Modular High Temperature Gas Reactor
NGNP	Next Generation Nuclear Plant
NRC	Us Nuclear Regulatory Commission
OSU	Oregon State University
P-LOFC	Pressurized Loss of Forced Convection
PCC	Pressurized Conduction Cooldown
PIRT	Phenomenon Identification and Ranking Table
SRQ	System Response Quantity
TAMU	Texas A&M University
VHTR	Very High Temperature Gas Reactor

Nomenclature

a	Cross-Sectional Area	M	Mass [kg] or Molar mass [kg/mol] or Set
A	Surface area	\dot{m}	Mass flow rate
Bo^*	Buoyancy parameter	N	No. of components or channels
C	Constant of proportionality	O	Subset
c_p	Constant pressure specific heat	p	Pressure
d	Diameter	Q	Volumetric flow
d_h	Hydraulic diameter	Q'''	Power density
D	Gas diffusion coefficient	q	Power
DF	Distortion factor	r	Radial dimension
f	Darcy friction factor	R	Universal gas constant
g	Acceleration of gravity	S	Source/sink of conserved property
Gr^*	Grashof number based on heat flux	t	Time
h	Heat transfer coefficient	T	Temperature
j	Flux of conserved property	u	Velocity
k	Thermal conductivity	V	Volume
K	Form loss coefficient	w	Gas molar velocity
K_v	Acceleration parameter	X	Mole fraction
l	Length	x	Wall thickness
L	Distance/Length/Vessel Length/ Height	z	Vertical or axial dimension

Non-Dimensional Ratios

Name	Notation	Formula	Interpretation in Terms of Ratio
Bi	Biot Number	$\frac{hd}{k_s}$	$\frac{\text{Surface Conductance}}{\text{Internal Conduction of Solids}}$
Gr	Grashof Number	$\frac{g\beta\Delta Td^3}{\nu^2}$	$\frac{\text{Buoyancy Force}}{\text{Viscous Force}}$
Nu	Nusselt Number	$\frac{hD}{k}$	$\frac{\text{Temperature Gradient at Wall}}{\text{Overall Temperature Difference}}$
Pe	Peclet Number	$\frac{V\rho C_p d}{k}$	$\frac{\text{Heat Transfer by Convection}}{\text{Heat Transfer by Conduction}}$
Pr	Prandtl Number	$\frac{\mu C_p}{k}$	$\frac{\text{Diffusion of Momentum}}{\text{Diffusion of Heat}}$
Re	Reynolds Number	$\frac{\rho V d}{\mu}$	$\frac{\text{Inertia Force}}{\text{Viscous Force}}$
Ri	Richardson Number	$\frac{g\beta\Delta Td}{\nu^2}$	$\frac{\text{Buoyancy Force} * \text{Viscous Force}}{\text{Inertia Force}}$

Greek Symbols

α Thermal diffusivity [m^2/s]	ν Kinematic viscosity [m^2/s]
β Thermal expansion coefficient [$1/\text{K}$]	ν_t Turbulent kinematic viscosity [m^2/s]
δ Thickness or pitch [m]	Π Characteristic time ratio
Δ Difference	ρ Density
ε Emissivity	σ Stefan-Boltzmann constant [$\text{W}/(\text{m}^2\text{K}^4)$]
θ Angular dimension	τ Time constant [s]
κ_m Mass diffusion coefficient [m^2/s]	Ψ Conserved property
κ_t Turbulent mass diffusivity [m^2/s]	ω Specific frequency [s^{-1}]
μ Dynamic viscosity of gas [$\text{N}\cdot\text{s}/\text{m}^2$]	

Subscripts, Superscripts, and Other Symbols

+	Non-dimensional	j	Jet or index
0	Reference (initial or maximum)	J	Index "j" maximum
amb	ambient	k	Constituent "k"
avg	Average	kn	Between constituent "k" to constituent "n"
b	Half-radius	L	Length
Brk	At break	LP	Lower plume
C	Cool gas	M	Model
c	Jet centerline	max	Maximum
cv	Control volume	NC	Natural convection
d	Diameter	NO	Normal operations
diff	Diffusion	OPM	Outlet plenum mixing
EF	Exchange flow	P	Prototype
F	Frictional resistance	r	radial dimension
G	Geometry	R	Ratio
g	Gas	sk	Source or sink
H	Upper plume or horizontal or Hot gas	TC	Thermal centers
i	Index	uc	Upcomer
1	Index "i" maximum	V	Vertical
IP	Inlet plenum	w	Wall
IPM	Inlet plenum mixing	z	Axial dimension

Abstract

Using experiments designed to provide data to Validate High-Fidelity and Systems Analysis Numerical Models to enhance understanding of Integral System Experiment Behavior and the Adequacy of Analysis Tools

Abstract--Idaho State University (2018)

The Very High Temperature Gas Reactor (VHTR) has been designated to be the Next Generation Nuclear Power Plant (NGNP) by the US Department of Energy (DOE). The licensing process of NGNP will include the analyses of different thermal-hydraulic phenomena using advanced high-fidelity multi-physics tools. These tools require prior validation which is performed employing low-distribution density vintage data in conjunction with high-distribution density advanced data. Such data are generated in separate effect tests alongside integral tests which are performed as a requirement of the validation pyramid. Appropriate scaling relationships are developed to provide links between such data measured in integral/separate-effects facilities and the prototype. Scaling distortions are also measured and quantified properly, so that the analysis tool used, to calculate the phenomena measured in the scaled facilities, can also adequately represent the phenomena behavior in the prototype for the scenario of interest.

Key Words: validation, vintage data, advanced data, data superposition, validation pyramid, integral effect tests, separate effect tests, scaling relationship analysis, upper plenum jet impingement, lower plenum mixing, laminarization, Richard Schultz, H2TS, LOFC, PLOFC, HTTF, MIR, MHTGR, HTGR, VHTR, NGNP

1. Introduction

There are different types of mathematical codes available nowadays. In the field of thermal hydraulics, such codes may be divided into two categories, a) system analysis codes like RELAP, TRACK, TRACE, CATHARE, etc. b) advanced high-fidelity multi-physics codes like Fluent, STAR-CD, COMSOL, etc. Every mathematical/ numerical code irrespective of its type or purpose, requires validation before commercialization or being accepted by the concerned user community.

The validation process determines the degree to which a mathematical/numerical model (and its associated data) is an accurate representation of the real world from the perspective of the intended uses of the mathematical model. The fundamental strategy of validation involves identification and quantification of the error and uncertainty in the conceptual and computational models, quantification of the numerical errors in the computational solution, estimation of the experimental uncertainty, and finally, a comparison between the computational results and the experimental data.

Unlike traditional experiments, the validation experiments emphasize on precisely measuring the conditions of an uncontrolled experiment rather than control and repeatability of the experiment. Variability in the surroundings of a validation experiment is not critical, as long as the conditions of the surroundings are precisely measured. For experiments with uncontrolled conditions, however, a number of experimental realizations are necessary to carefully characterize the variability of the system and surroundings so that this information can be provided for analysis.

During the validation process, one must address the associated uncertainties involved in the validation experiments. Two types of uncertainties that are addressed during validation a) epistemic uncertainty b) aleatory uncertainty. Epistemic uncertainty stems from lack of knowledge, thus simply an increase in knowledge or information can lead to a reduction in epistemic uncertainty. Aleatory uncertainty, on the other hand, occurs due to randomness. Aleatory uncertainty can be embodied in two ways in computational analyses: in the model form itself and in parameters of the model. If the model is given by a differential operator, then

aleatory uncertainty in the model form can be expressed as a stochastic differential operator. Aleatory uncertainty in parameters can occur in the mathematical description of the system and its characteristics, initial conditions, boundary conditions, or excitation function.

Measurement uncertainty is a form of aleatory uncertainty that mainly results from limitation in the data collection process during an experiment. This limitation exists especially in vintage data collection process which uses traditional intrusive instrumentation like thermocouples, pressure transducers etc. Data collected using traditional instruments have randomly distributed quantities that may take on values in a known range, but the exact value will vary from unit to unit, point to point in space, or time to time. The distribution density of vintage data is much lower, as the data collection process uses much coarser discretization i.e. control volume is much larger compared to the advanced data collection process. Traditional instrumentation has low distribution density due to the fact that they are intrusive i.e. if used in large quantities, they may affect the very experimental data which they are intended to attain. Another reason is that they may also diminish boundaries between system and surrounding by compromising the structural integrity. Lack of distribution density in vintage data engenders measurement uncertainty.

Advanced data collection process involves advanced instrumentation which uses optical/laser diagnostics techniques like particle image velocimetry (PIV) or laser doppler velocimetry (LDV). Despite the fact that these are non-intrusive, provide high-distributed density of data, and help to minimize measurement uncertainty; such instrumentation cannot be adopted for very high temperature experimental conditions as refractive index tend to vary with temperature.

In case of complex thermal-hydraulics phenomena like flow characteristics in passages at high temperature/pressure conditions, advanced instrumentation can be used to obtain high-distribution density data from separate effect tests at normal temperature/pressure conditions. These data, later on, can be used to validate high-fidelity multi-physics codes through data superposition technique by developing appropriate scaling relationships between the normal experimental conditions and high temperature/pressure conditions. Also, low-distribution density data are collected using traditional instrumentation at high temperature/pressure

experimental conditions. These vintage data in combination with high-distribution density advanced data may be used to further validate advanced high-fidelity multi-physics codes like CFD.

U.S. Nuclear Regulatory Commission's Regulatory Guideline (RG1.203) has outlined a protocol which consists of the following four elements for validation of a numerical model. Successful completion of four elements leads to acceptance of the numerical model.

Element-1 establishes requirements for numeric modeling capabilities and boundary conditions. The plant type, geometry, components, component regions, desired operating conditions, and most challenging transient and accident conditions are also identified. The figures-of-merit are used to evaluate the system safety and also the key phenomena for the system envelope are defined usually via the creation of the phenomena identification and ranking table (PIRT). Finally, the material properties of the system combined with the anticipated operational, transient, and accident conditions enable the required calculational accuracy to be prescribed in the context of the system licensing and operational requirements.

Element-2 develops validation database through performing experiments and using prescribed scaling methodologies, techniques, and the system envelope defined in Element-1. The experimental uncertainties are also identified. The development of the scaling equations sets and the calculational domain are boundary conditions for prescribing the required numeric models in Element-3. The validation matrix is defined using a validation triangle approach where the need for nuclear power plant data are built upon data obtained in scaled integral effects experiments, scaled separate effects experiments, and fundamental data.

Element-3 develops numeric models incorporating transport equations and required closure models to calculate the system behavior. The numeric models are tailored to be applicable, with the desired degree of calculational uncertainty, within the calculational domain described in Element 2.

Element-4 assesses numeric model using bottom-up and top-down approach to determine their adherence to the desired objectives. The top-down scaling approach evaluates the global system behavior and systems interactions from integral test facilities that can be shown to represent the plant-specific design under consideration. The bottom-up scaling analyses address issues raised in the plant and transient-specific PIRT related to localized behavior.

Key ingredients needed to assess the adequacy of the numeric models are the completion of the specification of the system envelope, development of the scaling equations, development of the calculational envelope, assessment of the calculational accuracy requirements, and development of the validation matrix. Following completion of the four elements, an adequacy decision is made using an accepted methodology.

A validation metric measures the difference between a System Response Quantity (SRQ) obtained from a simulation and one obtained from experimental measurements. Each validation matrix is unique to the plant geometry which deals with a set of operational and accident scenarios. For each individual scenario, key phenomena and figures-of-merit are identified. Full-scaled facilities can't be tested under very detrimental conditions. Full-scale tests are only performed for adverse conditions for selected components. The key to constructing the validation matrix is to design a comprehensive set of experiments, of the types shown in the validation pyramid displayed in Figure 1, which provide validation data for the challenging scenarios that must be analyzed to license the plant.

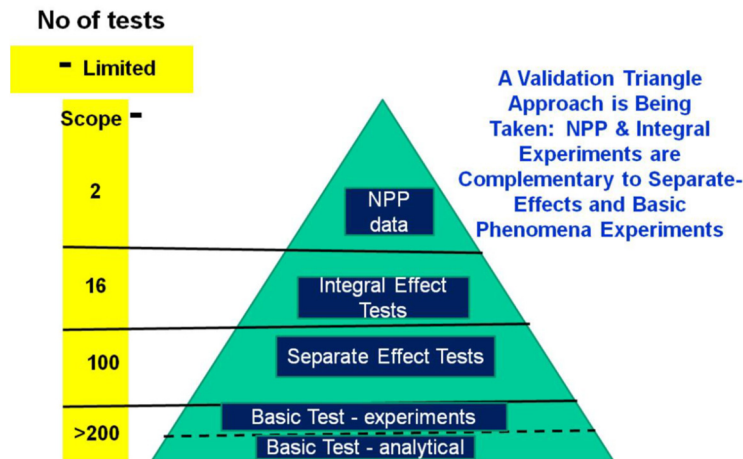


Figure 1: Typical Validation Pyramid

The data for each experiment must be scaled to the subject plant using a rigorous methodology that ensures the experimental data are related directly to the plant for nondimensional parameters that represent the key phenomena. One of the most important methodologies for producing a rigorous linkage between the validation data and the nuclear plant is that designed by Zuber and called the Hierarchical Two-Tiered Scaling (H2TS) Methodology. In essence, the methodology decomposes and organizes the system starting with the whole system, working downward through subsystems, components until reaching the transfer processes. Scale measures are assigned at each level. The lowest level transfer processes are characterized by the rate of transfer—a temporal scale and transfer area (spatial scale).

The US Department of Energy (DOE) has determined that the Next Generation Nuclear Plant (NGNP) will be the Very High Temperature Gas Reactor (VHTR). It has lower power density (8.4 KW/L) than LWRs (52 BWR, 105 PWR), uses helium as coolant and graphite as its moderator. Huge chunk of graphite works as a heat sink allowing for safer operation at higher temperatures which leads to higher operating efficiency of 39% compare to LWR efficiency of 33%. The United States Nuclear Regulatory Commission (NRC) is responsible for licensing and regulation of NGNP. Development of PIRT is the first step in scaling methodology. NGNP PIRT was completed for the NRC in 2008 (Ball et al. 2008). The validation matrix for the NGNP is based on the key scenarios identified in PIRT. Experimental data for validation purpose will be generated from conducting separate effect tests in different facilities alongside integral effect tests. In this report, we will consider the following scenarios to perform scaling studies - i) flow distribution and heat transfer during PCC ii) upper plenum jet impingement during pressurized conduction cooldown (PCC) iii) flow distribution and heat transfer during normal operational conditions iv) lower plenum jet impingement and hot streaking during normal operational condition. Hierarchical two-tiered scaling methodology will be used to scale the separate-effects facility. The following experimental facilities will be used as the basis for a case study in this research:

- a. Temperature Test Facility (HTTF) at Oregon State University (OSU) High—an integral test facility using traditional instrumentation and designed to study both operational and accident scenarios for the MHTGR.

c. City College of New York (CCNY) Core Heat Transfer Facility—a separate-effects experiment designed to study the flow and heat transfer behavior in the core region of the MHTGR under both operational and accident conditions using a simulated cooling channel and a bypass channel. Traditional instrumentation is used.

d. Texas A&M University Upper Plenum Mixing Facility—a separate-effects experiment designed to study the jet/plume behavior in the upper plenum of the MHTGR under accident conditions. Advanced instrumentation is used.

e. Matched-Index-of-Refractive (MIR) Facility at Idaho National Laboratory (INL)—a separate-effects experiment designed to study the flow behavior in the lower plenum of the MHTGR under operational conditions. Advanced instrumentation is used.

1.1 Goal of this research

Investigate how high-fidelity, intrusive, low-distribution density, vintage data obtained using traditional instrumentation may be used in conjunction with high-fidelity, nonintrusive, high-distribution density data using advanced instrumentation to validate advanced high-fidelity multi-physics analysis tools.

2. Objectives and Approach

- Identify the boundary conditions and requirements necessary to link databases in similar but differently scaled experimental separate-effects and integral-effects facilities. Discuss the strengths and theoretical limitations of the linkages between such facilities.
- Based on the key phenomena and figures-of-merit (FOM) identified in the U.S. Nuclear Regulatory Commission’s sponsored phenomena identification and ranking tables (PIRTs) for operational conditions and the pressurized loss-of-forced convection (PLOFC): identify the key scaling relationships between the facilities identified in the Introduction.
- Calculate the key scaling relationships for the above facilities and the scenarios-of-interest.
- Compare the key scaling relationships for the above facilities/scenarios and quantify the scaling distortions. Formulate conclusions regarding the usefulness and adequacy of this approach.

3. Description of the Experimental Facilities

Among the facilities, MHTGR is the prototype which will be built after the successful completion of the validation process. Then there is the HTTF integral facility located at OSU, which is 1/4-scale in both the height and radial dimensions to the MHTGR. HTTF will simulate various transient scenarios identified in PIRT. The CCNY, MIR, and TAMU experimental facilities will be used to run separate effect tests. Data from such tests will be linked together through the development of appropriate scaling relationships and thereafter be used to validate advanced high-fidelity codes.

3.1 Modular High Temperature Gas Reactor (MHTGR)

The MHTGR prismatic core design consists of prismatic graphite blocks. The fueled core region is annular and surrounded by an inner and outer reflector. The fuel consists of TRISO coated fuel particles, which are embedded into graphite compacts. These graphite compacts are then placed in prismatic graphite blocks which are located in the core region. The inner and outer reflectors are composed of unfueled prismatic graphite blocks.

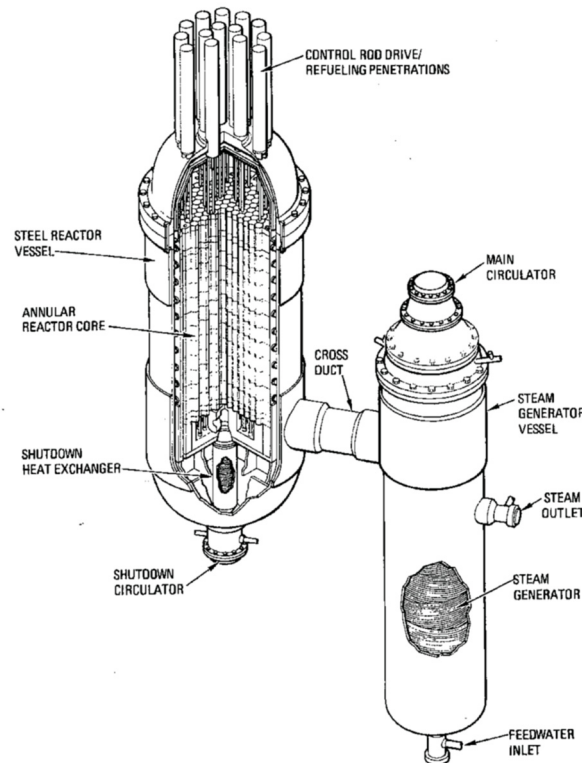


Figure 2: MHTGR Module (DOE 1986)

During normal operation, the maximum fuel temperature is designed to be less than 1100°C. The maximum design fuel temperature during an accident is approximately 1600°C. Figure-2 shows a cut away schematic of the prismatic block MHTGR design. The coolant is gaseous helium. Helium flows into the vessel by way of a concentric core inlet-outlet duct. The helium enters the vessel at approximately 259°C and 6.4 MPa. The gas enters upcomer channels located in the gap between the inner vessel wall and the metallic core barrel surrounding the permanent side reflector. The flow in this region is of importance since the cooler helium helps to maintain the vessel wall temperature below prescribed limits. Once exiting the upcomer the flow enters the upper plenum. The upper plenum region walls are insulated in order to protect the upper plenum from hot gas flows during a pressurized conduction cooldown event. The gas then flows downward through the upper core supports and into the fuel elements and coolant channels in the prismatic blocks.

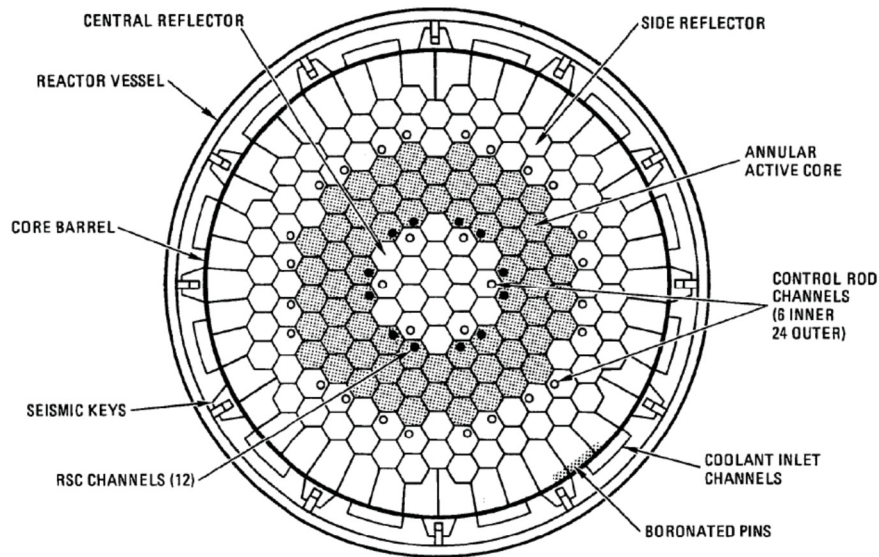


Figure 3: Plan view of reactor vessel and internals in an elevation through the core region (DOE 1986)

A fraction of the coolant flow is to be considered bypass flow in the sense that it flows through gaps between fuel element graphite blocks. The presence of bypass flow and a variety of axial peaking factors in different blocks and channels allows for a range of channel outlet temperatures into the lower plenum. Figure-3 shows a cross-sectional view of the fuel annulus and the inner and side reflectors. The average temperature rise across the core is approximately 428°C for the

MHTGR. For the MHTGR design, this allows for an approximately 687°C, well mixed, helium outlet temperature. Since there are variations in gas temperature as the gas exits the individual core channels there may be gas streams that have temperatures higher than 687°C. The lower plenum walls are insulated to avoid excessive wall thermal loads due to the impact of these high temperature streams. The maximum design temperature for the upper plenum shroud, core support structure and the core barrel in the MHTGR is 760°C.

3.2 High Temperature Test Facility (HTTF) at OSU

The High Temperature Test Facility (HTTF) at OSU is an integral test facility equipped with traditional instrumentation. It is 1/4-scale in both the height and radial dimensions to the Modular High Temperature Gas-Cooled Reactor (MHTGR) and will have electrically heated core (heater power of approximately 600 kW). It is a full temperature facility; thus the manufacturability of the vessel will then limit the HTTF vessel to a maximum pressure of 0.8 MPa. This decision is based on economics and safety limits for high-temperature pressure vessels. The facility is capable of operation at 850°C (well-mixed helium) with a maximum operating pressure of 0.8 Mpa. The facility is configured to simulate a variety of postulated depressurized conduction cool-down, pressurized conduction cool-down, and normal operations events.

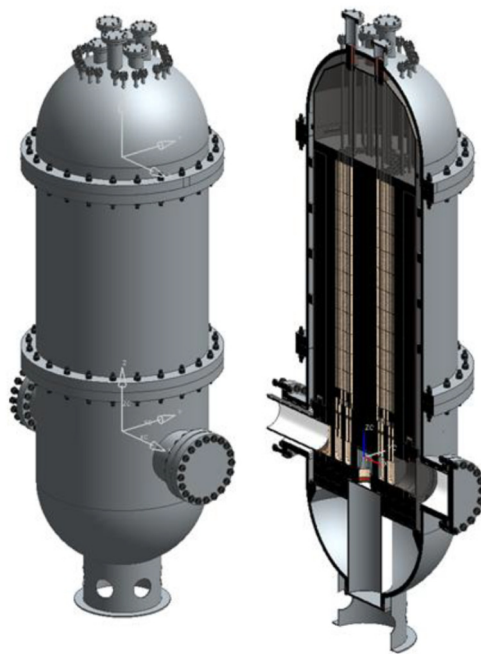


Figure 4: Oregon State University High Temperature Test Facility

the upper plenum. The experimental facility contains two main parts; the core and the upper plenum. The core is connected to the upper plenum, while the lower part is connected to the core inlet. Fluid flows from the reservoir to the bottom of the core via a pipe which is connected to a pump and a flowmeter. The flowmeter is connected to a Data Acquisition System (DAQ) to record and monitor the flowrates continuously.

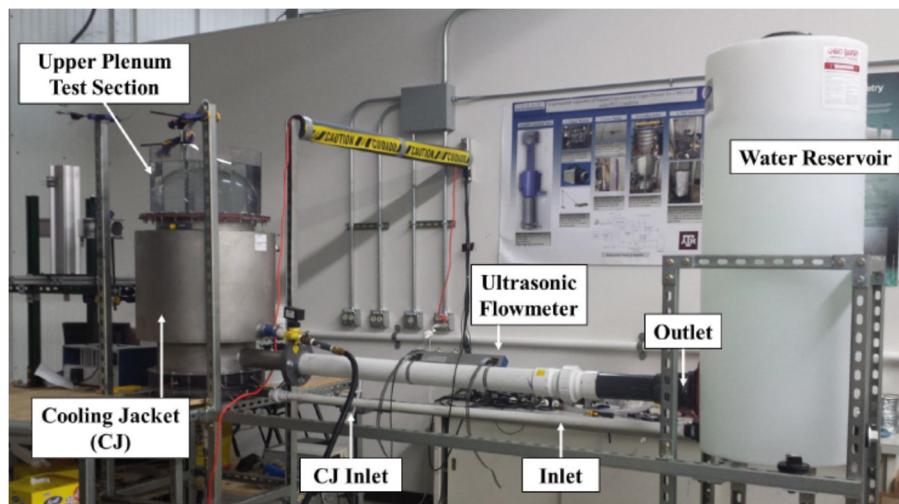


Figure 6: Upper Plenum Mixing Test Facility at TAMU

The upper plenum is made of polycarbonate material to provide access for the Particle Image Velocimetry (PIV) measurements. When a curved surface is filled with water, there is an optical distortion caused by refraction, complicating imaging of the plenum. Due to this, a correction box was built around the upper plenum. The correction box presents a flat viewing plane, and the medium between the plane and curved surface is filled with water so that the images may be recorded without refraction. Only a single jet was considered to generate a reference experimental data of jet impingement on the upper plenum. The recorded data will be used to validate high-fidelity analysis tools.

3.5 Matched Index of Refraction (MIR) Facility at INL

The Matched Index of Refraction (MIR) facility consists of flow channels inside quartz structure. The working fluid is mineral oil at controlled room temperature. The quartz components having the same refractive index as mineral oil can barely be seen. The measurements reveal developing, non-uniform, turbulent flow in the inlet jets and complicated flow patterns in the model lower plenum. Advanced instrumentation such as laser Doppler velocimetry (LDV) and

particle image velocimetry (PIV) are used. Data include three-dimensional vector plots, data displays along the coordinate planes and presentations that describe the component flows at specific regions in the model.

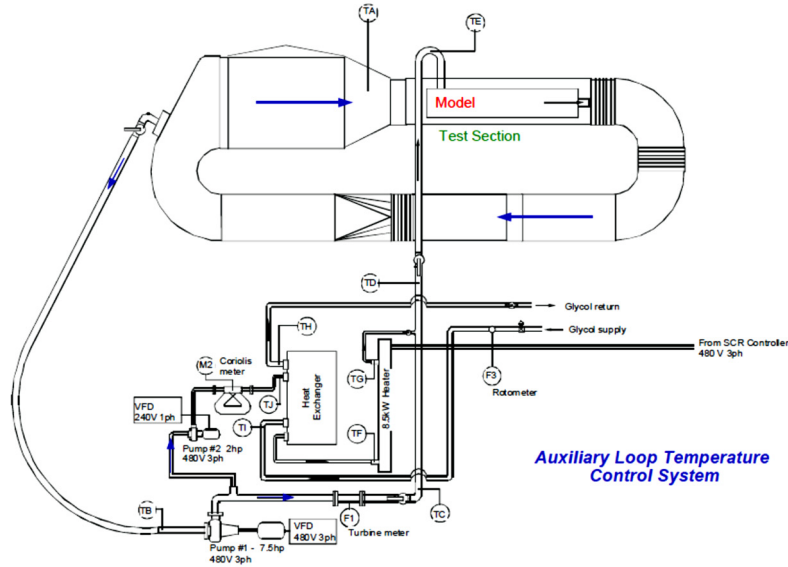


Figure 7: Schematic diagram of temperature control system for typical internal flow experiment in INL MIR flow system.

The “bypass flows” in a prismatic gas-cooled reactor are of potential concern because they reduce the desired flow rates in the coolant channels and, thereby, can increase outlet gas temperatures and maximum fuel temperatures. The purpose of the fluid dynamics experiments to be conducted in the INL MIR system is to develop benchmark databases for the assessment of CFD solutions of the momentum equations, scalar mixing, and turbulence models for geometries of Very High Temperature Reactors (VHTR) in the limiting case of negligible buoyancy and constant fluid properties. The MIR VHTR bypass flow experiment will measure flow characteristics in the coolant channels and interstitial gaps between typical prismatic blocks. The experiment is isothermal and can only be used to study momentum-dominated phenomena which are not affected by fluid density gradients. Thus the MIR can be used to study thermal-fluid behavior for operational conditions but not for natural convection conditions that will exist during the PCC and DCC scenarios. MIR hardware will be used to model mixing in the lower plenum, the interstitial bypass regions of the MHTGR. The data provided by the MIR experiment are for validation of high-fidelity codes.

4. Hierarchical 2-Tiered Scaling (H2TS) Analysis Method

There are four basic elements of the H2TS analysis method. The first element consists of subdividing the plant into a hierarchy of systems. Each system is subdivided into interacting subsystems which are further subdivided into interacting modules which are further subdivided into interacting constituents (materials) which are further subdivided into interacting phases (liquid, vapor or solid). Each phase can be characterized by one or more geometrical configurations and each geometrical configuration can be described by three field equations (mass, energy and momentum conservation equations). Each field equation can incorporate several processes.

The second element consists of identifying the scaling level at which similarity criteria should be developed. This is found by examining phenomena. For example, if mass, momentum, or energy transfer is between two materials then the scaling criteria should be developed at the coolant level. If mass, momentum, or energy is between two phases of same material then the scaling criteria should be developed at the phase level.

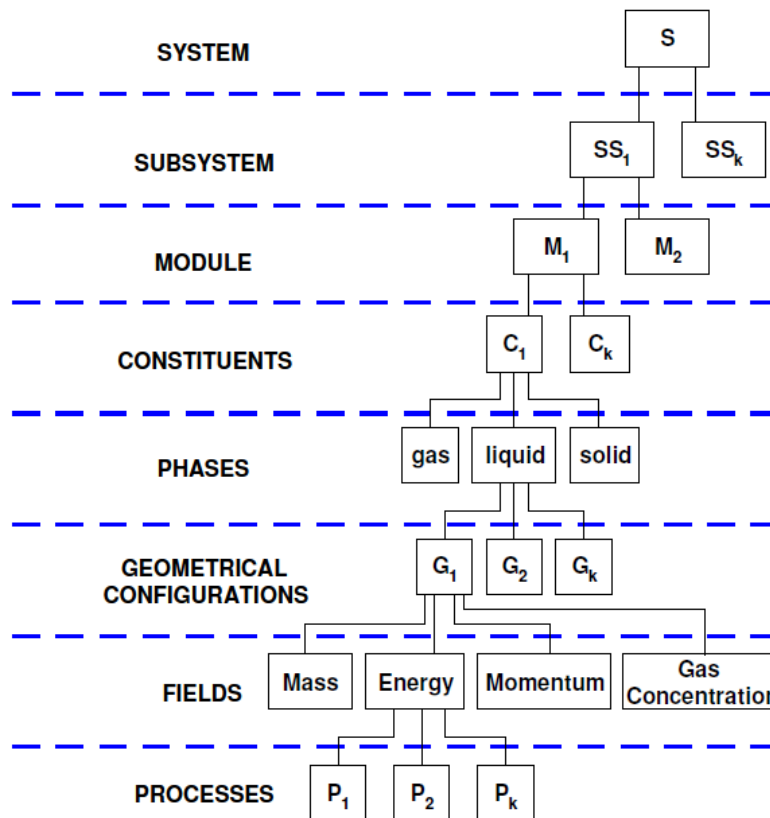


Figure 8: General Approach for System Breakdown in the H2TS Methodology

The third element consists of performing a top-down (system) scaling analysis. This analysis addresses the effects on a system caused by the interaction of its constituents, which have been identified as important in the Phenomena Identification and Ranking Table (PIRT). In this step, similarity criteria will be developed. Processes to be addressed in the bottom-up scaling will also be identified.

The fourth element of the H2TS analysis method is the bottom-up scaling analysis. In this step, similarity criteria are developed for the specific processes of importance as identified in the PIRT.

The specific objective of the H2TS methodology is to set up characteristic time ratios for transfer processes of interest. In order to achieve this, control volume balance equations are written for each constituent "k" as follows:

$$\frac{dV_k\psi_k}{dt} = \Delta[Q_k\psi_k] \pm \sum [j_{kn}A_{kn}] + S_k \dots\dots\dots (4.1)$$

In this equation, ψ_k is the conserved property such as mass (ρ), momentum (ρu) and energy (e) per unit volume. V_k represents the control volume and Q_k the volumetric flow rate. $j_{kn}A_{kn}$ is the transport process transfer term for phenomena such as condensation where j_{kn} is the flux of the conserved property transferred from constituent "k" to constituent "n" across transfer area A_{kn} . S_k accounts for the distributed sources (such as body forces) or sinks acting on the control volume. The first term on the right-hand side (RHS) of the equation shows the convective flux of the conserved property and can be described using the following equation:

$$\Delta[Q_k\psi_k] = [Q_k\psi_k]_{in} - [Q_k\psi_k]_{out}$$

Equation 2.1 can be written in a non-dimensional form by using the following non-dimensional properties in terms of the initial and boundary conditions of the system.

$$V_k^+ = \frac{V_k}{V_{k,0}}$$

$$\psi_k^+ = \frac{\psi_k}{\psi_{k,0}}$$

$$Q_k^+ = \frac{Q_k}{Q_{k,0}}$$

$$j_{kn}^+ = \frac{j_{kn}}{j_{kn,0}}$$

$$A_{kn}^+ = \frac{A_{kn}}{A_{kn,0}}$$

$$S_k^+ = \frac{S_k}{S_{k,0}}$$

Substituting these non-dimensional properties into equation 2.1 yields a non-dimensional form of the control volume balance equation.

$$V_{k,0}\psi_{k,0} \frac{dV_k^+\psi_k^+}{dt} = Q_{k,0}\psi_{k,0}\Delta[Q_k^+\psi_k^+] \pm \sum [j_{kn,0}A_{kn}] [j_{kn}^+A_{kn}^+] + S_{k,0}S_k^+$$

Dividing above equation by $Q_{k,0}\psi_{k,0}$ yields:

$$\tau_k \frac{dV_k^+\psi_k^+}{dt} = \Delta[Q_k^+\psi_k^+] \pm \sum \Pi_{kn} [j_{kn}^+A_{kn}^+] + \Pi_{sk}S_k^+ \dots\dots\dots (4.2)$$

In equation 2-10, the residence time of constituent "k" is given by:

$$\tau_k = \frac{V_{k,0}}{Q_{k,0}}$$

The characteristic time ratio for transfer processes between "k" and "n" is given by:

$$\Pi_{kn} = \frac{j_{kn,0}A_{kn}}{Q_{k,0}\psi_{k,0}}$$

and the characteristic time ratio for the distributed source (or sink) term within the control volume is given by:

$$\Pi_{sk} = \frac{S_{k,0}}{Q_{k,0}\psi_{k,0}}$$

Each process characteristic time ratio can be ranked by importance by comparing the time ratios. This is crucial since it identifies the specific processes that have the same effect in the prototype and the model.

It may be possible to preserve a subset of the characteristic time ratios between model and prototype so that the following equation is true for the most important processes.

$$O_P[\Pi_{i,j}] = O_M[\Pi_{i,j}] \cdots \cdots \cdots (4.3)$$

This allows the modeler to optimize the model design to preserve similarity in the most important processes and to allow for distortion in the processes of less importance. In order to determine which processes govern a transient, numerical estimates of the characteristic time ratios for both the prototype and the model can be made at the hierarchical levels of interest. The degree to which a specific transfer process could impact the transient can be determined by comparing the maximum characteristic time ratios for each of the transfer processes present during the transient.

Physically, each characteristic time ratio is composed of two specific parts as shown in equation following equation, represents the specific frequency, which is an attribute of the specific process and quantifies the mass, momentum, and energy transfer rates for the process. τ_{cv} represents the resident time constant for the control volume which is the total time available for the process to occur.

$$\Pi_i = \omega_i \tau_{cv}$$

Processes, where Π_i is much smaller than one, are typically processes of limited importance in the transient since only a small amount of the conserved property will be transported in the limited time available during the transient. Processes where Π_i is approximately equal to or greater than one evolve at a high enough rate so that a significant amount of the conserved property can be transferred during the transient. This type of process would be considered to be important to the overall transient behavior.

A set of characteristic time ratios (dimensionless Π groups) and similarity criteria for each mode of operation must be developed. It is impossible to satisfy all criteria for all modes of operation and thus the facility design is optimized to preserve the most important processes as identified in the PIRT and the development of the time ratios such that equation 2.3 is satisfied. This optimization occurs by adjusting the physical geometry, fluid properties, operational conditions and boundary conditions of the model.

Because similarity criteria for all characteristic time ratios will not be satisfied, an analysis of scaling distortions should be conducted. A distortion factor which quantifies the fractional difference in the amount of conserved property transferred through the evolution of a specific process in the prototype with the amount of conserved property transferred through the same process in the model during their respective residence times is defined in the following equation.

$$DF = \frac{[\Pi_i]_P - [\Pi_i]_M}{[\Pi_i]_P} \dots \dots \dots (4.4)$$

A distortion factor of zero would indicate that the model ideally simulates the specific process. A distortion factor of +0.05 would indicate that the specific process in the model transfers 5 percent less of the conserved property (on a scaled basis) than the same process in the prototype.

Once the characteristic time ratios have been developed and distortions quantified, a set of design specifications for each mode of operation can be prepared. Key thermal hydraulic processes must be evaluated in order to prioritize these design specifications. Finally, the prioritized design specifications are integrated into a set of specific facility design requirements.

5. Pressurized Conduction Cooldown Events

PCC may occur due to complete loss of flow accident or from a break between the inlet and outlet duct. During the PLOFC event, there is a loss of forced convection through the core but the system integrity is maintained so that the pressure during the event remains close to normal operating pressures. During normal operation, helium enters the upper plenum through the upcomer, then moves downward into the core into the lower plenum. In case of a PCC however, the buoyancy forces of the coolant become greater than the inertia and gravitational forces which will cause flow reversal. With natural convection in place, the coolant will flow upwards through the core (Figure-9) and temperature reverses which is opposite of the flow route during normal operation. During this event, natural convection is the primary heat transfer mechanism within the core. With the hottest coolant exiting the top of the core into the upper plenum, the top of the vessel tends to become the hottest region of the vessel. The following phenomena during PLOFC event will be studied as “separate effect tests” at CCNY and TAMU test facilities.

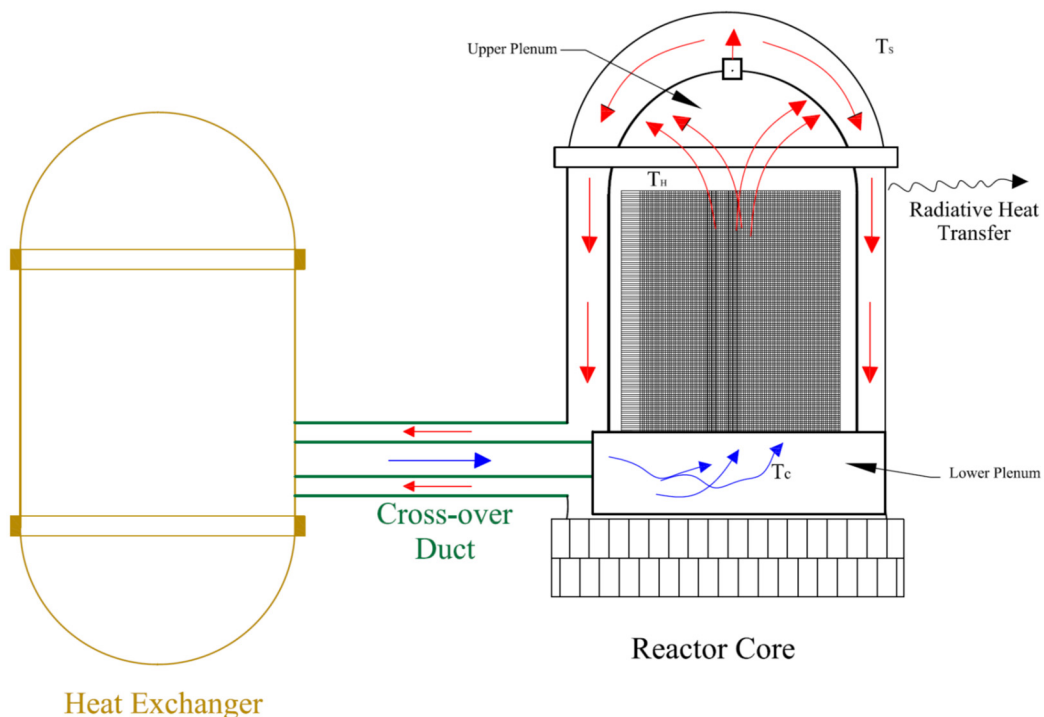


Figure 9: Single-Phase Natural Circulation

Intracore natural circulation is also a possibility where flow moves upward through the high temperature cooling channels located at the center of the core and moves downward via comparatively low temperature cooling channels located at the periphery of the core. This phenomena is shown in the following diagram (Figure 10).

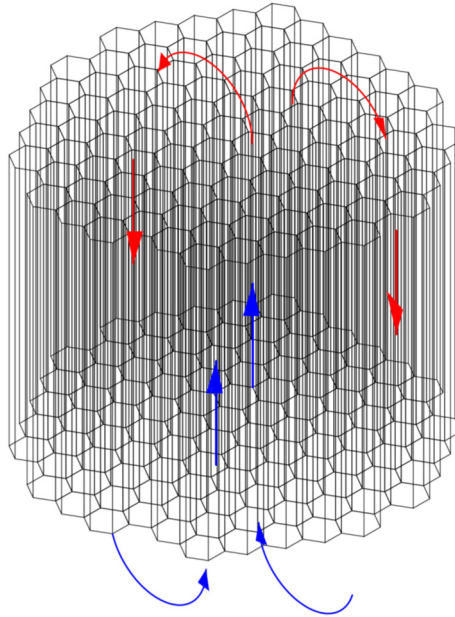


Figure 10: Intracore Natural Circulation

5.1 Flow distribution and heat transfer

During PLOFC, the flow sequentially changes from high-Reynolds-number turbulent regime, through low-Reynolds-number turbulent & laminarization regime, to laminar flow both upwards and downwards driven by buoyancy forces. At the laminarization regime; flows which are expected to be turbulent i.e. having Reynolds numbers above the critical Reynolds number or even transition flow; show heat transfer parameters as low as in laminar flows.

There are a number of components of the PLOFC phenomenon which add to the uncertainty of its quantification such as (1) low flow correlations, (2) flow reversal phenomena, (3) core coolant bypass flow, and (4) coolant flow friction and viscosity effects. The maximum fuel temperature of the reactor core in such case is directly correlated to the buoyancy-driven heat transfer within the core and outside the reactor vessel. The CCNY facility is intended to determine the flow behavior and heat transfer effects. Key parameters for analysing such phenomena would include

the Reynolds number, Prandtl number, q^+ (non-dimensional heat flux), Bo^* (buoyancy), and K_v (acceleration parameter).

5.2 Upper plenum jet impingement

When flow reversal occurs, natural convection will take place within the core. The gas jets within the channel will have different temperatures and velocity profiles depending on various decay heat. The decay power and the bypass flow are anticipated to be major contributors to this phenomenon. The impact of jet impingement on the upper plenum will be studied at the TAMU test facility. The flow at the inlet of the upper plenum experiences heavy fluctuations. This is an indication that the flow has higher turbulence intensity at the inlet. The maximum velocity at the inlet of the jet decreases until the flow hits the wall. After this, the wall-effect separates the flow in the mean radial velocity and flows down the wall of the upper plenum. Buoyancy, Reynolds number, & acceleration parameter play the significant role in developing scaling relationship between the facilities.

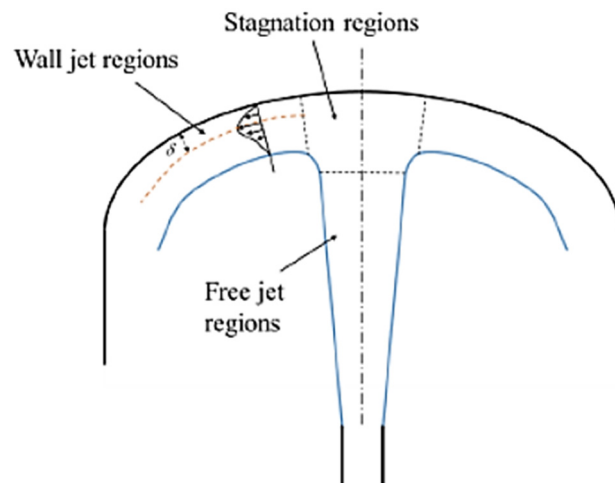


Figure 11: Axisymmetric Impinging Jet

6. Normal Operational Condition Events

Forced convection is the dominant heat transfer process during normal operation (Figure-12). There are several phenomena that primarily occur during normal operation i.e. while the forced convection is taking place; that could degrade the structure and components of the vessel and core to a point where these structures and components may not work as designed when challenged during an accident scenario. The following phenomena during operational condition will be studied as “separate effect tests” at the CCNY and MIR test facilities.

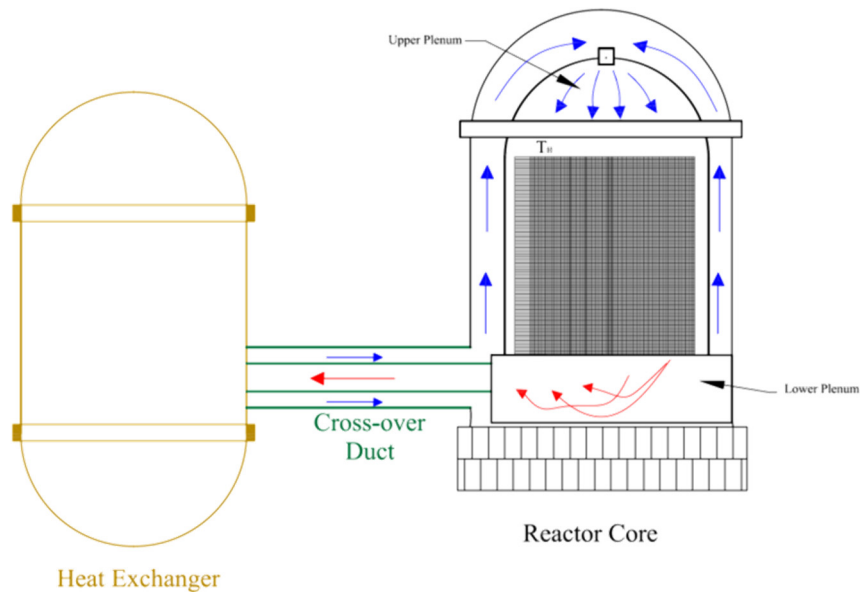


Figure 12: Normal Operational Condition

6.1 Coolant, bypass flow, and temperature distribution

Convection heat transfer could be seriously degraded due to the flow “laminarization” phenomenon in which turbulent flows having Reynolds numbers above the critical Reynolds number of $\sim 2,300$ or even transition flow Reynolds numbers of $2,300 - 4,000$ could exhibit low heat transfer coefficients typical of laminar flow. Poor convection heat transfer can then lead to high graphite block temperatures surrounding the coolant channels and “hot spots”.

Core coolant bypass flow represents the coolant which is not subject to direct core heating. It may be caused by flow between the gaps (spacers) in the graphite blocks for the prismatic block core design. The amount of bypass flow is a factor determining active convective cooling during normal operation and thus it will affect the maximum fuel temperature in the core during normal

operations. Maximum fuel temperatures significantly higher than currently anticipated may lead to fuel degradation which could challenge the fuel integrity during an accident. This phenomenon is ranked high in importance and low in knowledge by the PIRT panel. The CCNY facility is built to study coolant flow behavior, bypass, and temperature distribution effects. Reynolds number, Prandtl number, and K_v (acceleration parameter) will mostly determine appropriate scaling relationships between separate effect tests and integral effect tests.

6.2 Lower plenum mixing and jet impingement

MHTGR uses pressurized helium as coolant to enhance the heat transfer process. A complex turbulent mixing takes place as the high-temperature coolant jets enter the lower plenum beneath the core. The temperature, momentum and turbulence profiles of the gas exiting the channels serve as initial conditions for the passages forming these jets. Poor mixing of the high-temperature jets that enter the lower plenum from the hottest coolant channels may damage metallic components from local "hot streaks". The design issue, in this case, is the need for predicting the rates of turbulent mixing occurring between the hotter coolant jets and the rest of the flow before these hot jets impinge on the metallic components at the exit or on the insulation layer on the floor of the core lower plenum (Figure-13). Jets are subjected to some cross flows coming from the further side of the core. As a result, a better mixing of jets takes place at the exit near the hot (crossover) duct due to the crossflow coming from the further side of the core.

In normal operation at high pressures, strong heating inside the core can induce laminar convection although the Reynolds numbers are well above the conventional critical Reynolds number of $\sim 2,300$. If the coolant flow remains laminar at the Reynolds numbers used in the core design, hot spots can readily occur due to poor convection heat transfer during laminar flow. Since the transition Reynolds number increases with the coolant pressure, the coolant flow under normal operation could experience laminar flow and hot spots due to significant heat transfer degradation.

During full power operation, forced convection is the dominant heat transfer mechanism within the core. Typical Reynolds numbers within the coolant passages in the graphite core are on the order of 50,000. Under these conditions, turbulent mixing is the predominant contributor to the heat transfer process and buoyancy or thermal radiation are of lesser importance. Hot jets

impinge on the metallic components located on the floor of the core lower plenum (Figure-13). The structural integrity of the lower plenum components may be affected by such impacts.

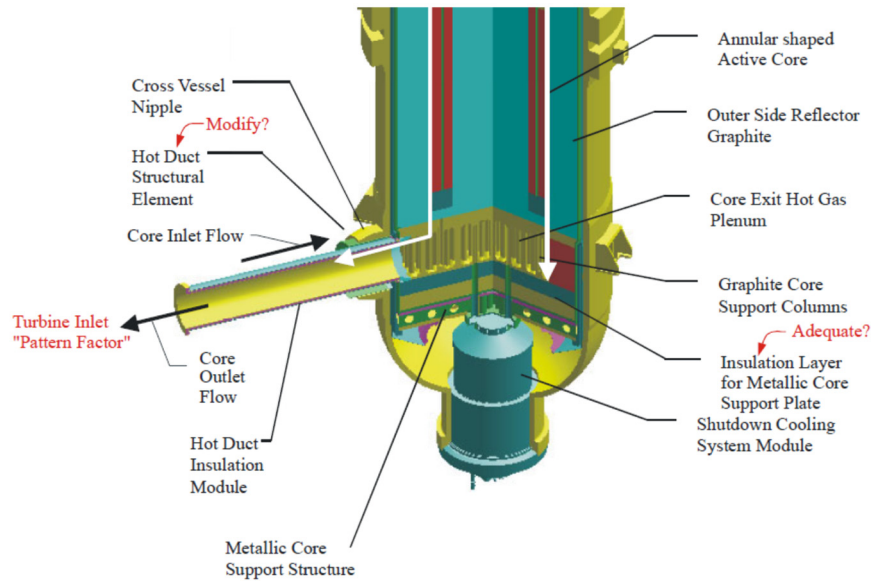


Figure 13: Relation of "hot channel" and "hot streaking" issues

The flow in the lower plenum can locally be considered to be a situation of multiple buoyant jets into a confined density-stratified crossflow with obstructions. Since the flow converges ultimately to a single outlet, the hot jets encounter different crossflow velocities depending on their locations relative to the outlet. The jets furthest from the outlet essentially exhaust into stagnant surroundings between the adjacent posts with the exception of the flow which they induce and some leakage flow. These furthest jets become wall jets (along the corner formed by prismatic outer reflector support blocks) that then impinge on the floor of the plenum. On the other hand, the last row of jets before the outlet encounters crossflow from all the other jets.

Due to the complexity of the flow path in the lower plenum and high temperature, it is not possible to use nonintrusive equipment to gather data from such experiments. Separate effect tests will be conducted at the MIR facility at room temperature. Locations of "hot streaks" that may question the structural integrity will be predicted from the data generated. These data will be used to validate advanced numeric models (like CFD codes). Reynolds number, q^+ (non-dimensional heat flux), Bo^* (buoyancy), and K_v (acceleration parameter) will play an important role in determining scaling relationship between MIR and MHTGR in this case.

7. Scaling Analysis of Pressurized Conduction Cooldown Event

During PLOFC event, localized natural circulation patterns are more likely to affect the heat transfer processes. Such localized phenomena encompass the mixing of hot gas jets exiting the top of the core or intra-core, intra-system natural circulation flow paths.

7.1 Single Phase Natural Circulation

The principal phenomenon of interest being investigated through this analysis is the single-phase natural circulation heat transfer in the core. This heat transfer will be important when examining the temperature profiles and peak fuel temperatures for the prismatic block core following a PCC event and after the onset of natural circulation. The objectives are to develop a solution for natural circulation flow rates for various core heat inputs and to develop similarity criteria for core and vessel transfer processes. Figure-14 provides a flow diagram that describes the scaling analysis process for this operational mode of the PCC event.

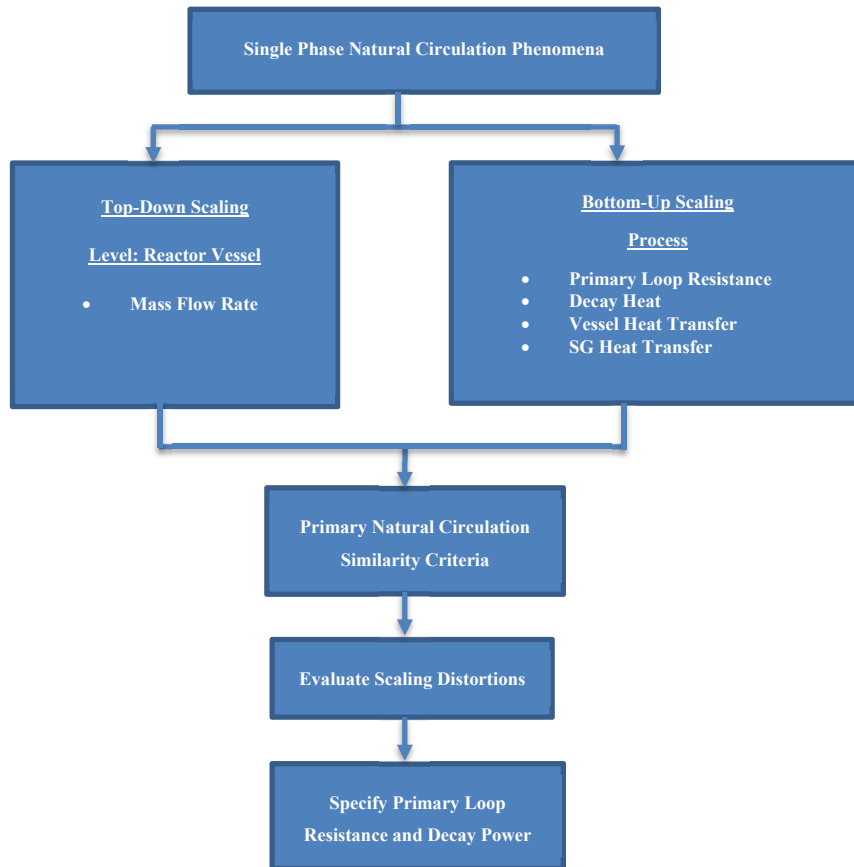


Figure 14: Scaling Analysis Flow Diagram for Single Phase Natural

First, a top-down scaling analysis was performed at the subsystem level. The purpose of the top-down scaling analysis was to scale the primary loop natural circulation mass flow rates.

Following the top-down scaling analysis, a bottom-up/process scaling analysis was performed to develop similarity criteria for the loop hydraulic resistance, the core decay power and heat transfer, and the steam generator heat transfer.

7.1.1 Single-Phase Natural Circulation Loop Scaling Analysis

The natural circulation phase of the transient begins following a loss of forced convection when the inertia of the gas flow is overcome by the buoyancy force created by gas heating in the core and flow reversal occurs. Cool helium enters the lower plenum and flows up through the core where it is heated to a temperature T_H . The helium may undergo significant expansion in the core region due to local heating. The hot helium flows into the upper plenum where it is cooled down via radiative heat transfer from the vessel head. The cooler gas then flows downward through upcomer risers and undergoes additional cooling due to vessel wall radiation and convection heat transfer. The helium then moves to the heat exchanger (steam generator) where the gas will be cooled further to T_C and undergo significant compression as the gas is cooled. A simple sketch of the natural circulation flow path under consideration is presented in Figure-09.

7.1.1.1 Governing Equations

Mass, momentum, and energy control volume balance equations can be written for each component within the system. Following assumptions are made for the PCC event analysis:

1. Flow is one-dimensional along the loop axis.
2. Fluid properties are uniform in each cross-section.
3. The fluid is incompressible. (Mach number < 0.3)
4. Pressure losses in the core dominate the loop resistance.
5. Viscous dissipation is negligible.

7.1.1.2 Dimensionless Balance Equations

Since the flow is considered as incompressible, the following equation can be used as the integrated loop momentum balance equation for the single-phase natural circulation phase:

$$\sum_{i=1}^N \left(\frac{l_i}{a_i} \right) \frac{d\dot{m}_{loop}}{dt} = g(\rho_{avg,C} - \rho_{avg,H})L_{TC} - \frac{(\dot{m}_{loop})^2}{2} \sum_{i=1}^N \left[\left(\frac{fl}{d_h} + K \right)_i \left(\frac{1}{\rho_i a_i^2} \right) \right]$$

In case of the loop energy balance equation, the rate of change of energy stored in the coolant is balanced against the energy added as the coolant flows across the core, the energy lost to the environment from the system, and the energy stored in the structural components of the vessel. The equation is shown below:

$$\rho c_p \frac{\partial T}{\partial t} + \rho c_p w \frac{\partial T}{\partial z} = k \frac{\partial^2 T}{\partial z^2} + q'''_{core} + q'''_{SG}$$

The set of governing equations can be made dimensionless by normalizing the terms relative to their initial conditions or boundary conditions. Dimensionless momentum and energy balance equations for the system loop are shown in equations (7.1) and (7.2). In this analysis, the height between the thermal centers of the steam generator and the core is used as the characteristic length. The characteristic density and temperature differences are taken as the difference between the helium density and temperatures at T_H and T_C . The characteristic time ratios that follow, the initial time is taken as the time of flow reversal and the onset of natural circulation.

$$z^+ = \frac{z}{L_{TC}}$$

$$w^+ = \frac{w}{w_{avg,core,0}}$$

$$k^+ = \frac{k}{k_{avg,core,0}}$$

$$\rho^+ = \frac{\rho}{\rho_{avg,core,0}}$$

$$c_p^+ = \frac{c_p}{(c_{p,avg,core})_0}$$

$$t^+ = \frac{t}{\tau_{NC}} = \frac{t w_{avg,core,0}}{L_{TC}}$$

$$\dot{m}_{loop}^+ = \frac{\dot{m}_{loop}}{\dot{m}_{loop,0}} = \frac{\dot{m}_{loop}}{\rho_{avg,core,0} a_{core} w_{avg,core,0}}$$

$$T^+ = \frac{T}{(T_{avg,H} - T_{avg,C})_0}$$

$$(q'''_{core})^+ = \frac{q'''_{core}}{(q'''_{core})_0}$$

$$(q'''_{SG})^+ = \frac{q'''_{SG}}{(q'''_{SG})_0}$$

$$(\rho_{avg,C} - \rho_{avg,H})^+ = \frac{(\rho_{avg,C} - \rho_{avg,H})}{(\rho_{avg,C} - \rho_{avg,H})_0}$$

$$\sum_{i=1}^N \left[\left(\frac{fl}{d_h} + K \right) \left(\frac{1}{p_i a_i^2} \right) \right]^+ = \frac{\sum_{i=1}^N \left[\left(\frac{fl}{d_h} + K \right) \left(\frac{1}{p_i a_i^2} \right) \right]}{\sum_{i=1}^N \left[\left(\frac{fl}{d_h} + K \right) \left(\frac{1}{p_i a_i^2} \right) \right]_0}$$

Substituting the above normalized parameters into the momentum equation:

$$\begin{aligned} & \sum_{i=1}^N \left(\frac{l_i \rho_{avg,core,0} a_{core}^2 w_{avg,core,0}^2}{a_i L_{TC}} \right) \frac{d\dot{m}_{loop}^+}{dt^+} \\ &= g L_{TC} (\rho_{avg,C} - \rho_{avg,H})_0 (\rho_{avg,C} - \rho_{avg,H})^+ - \sum_{i=1}^N \left[\frac{fl}{d_h} + K \right]_0 \\ & \quad * \frac{\rho_{avg,core,0}^2 a_{core}^2 w_{avg,core,0}^2 (\dot{m}_{loop}^+)^2}{p_i a_i^2} \sum_{i=1}^N \left[\left(\frac{fl}{d_h} + K \right) \left(\frac{1}{\rho_i a_i^2} \right) \right]^+ \end{aligned}$$

Dividing both sides by $\rho_{avg,core,0} w_{avg,core,0}^2$

$$\begin{aligned} & \sum_{i=1}^N \left(\frac{l_i a_{core}}{a_i L_{TC}} \right) \frac{d\dot{m}_{loop}^+}{dt^+} \\ &= \frac{g L_{TC} (\rho_{avg,C} - \rho_{avg,H})_0}{\rho_{avg,core,0} w_{avg,core,0}^2} (\rho_{avg,C} - \rho_{avg,H})^+ \\ & \quad - \sum_{i=1}^N \left[\frac{fl}{d_h} + K \right]_0 \frac{\rho_{avg,core,0} a_{core}^2 (\dot{m}_{loop}^+)^2}{p_i a_i^2} \sum_{i=1}^N \left[\left(\frac{fl}{d_h} + K \right) \left(\frac{1}{\rho_i a_i^2} \right) \right]^+ \end{aligned}$$

Which gives us the following Loop Momentum Balance Equation:

$$\begin{aligned} \Pi_{G,PCC} \frac{d\dot{m}_{loop}^+}{dt^+} &= \Pi_{Ri,PCC} (\rho_{avg,C} - \rho_{avg,H})^+ \\ &- \Pi_{F,PCC} \frac{(\dot{m}_{loop}^+)^2}{2} \sum_{i=1}^N \left[\left(\frac{fl}{d_h} + K \right)_i \left(\frac{1}{\rho_i a_i^2} \right) \right]^+ \dots \dots (7.1) \end{aligned}$$

Similarly substituting normalized parameters into the energy equation:

$$\begin{aligned} &\rho_{avg,core,0} (c_{p,avg,core})_0 (T_{avg,H} - T_{avg,C})_0 \frac{w_{avg,core,0}}{L_{TC}} \rho^+ c_p^+ \frac{\partial T^+}{\partial t^+} \\ &+ \frac{\rho_{avg,core,0} (c_{p,avg,core})_0 (T_{avg,H} - T_{avg,C})_0 w_{avg,core,0}}{L_{TC}} \rho^+ c_p^+ w^+ \frac{\partial T^+}{\partial z^+} \\ &= \frac{k_{avg,core,0} (T_{avg,H} - T_{avg,C})_0}{L_{TC}^2} k^+ \frac{\partial^2 T^+}{\partial z^+{}^2} + (q'''_{core})_0 (q'''_{core})^+ + (q'''_{SG})_0 (q'''_{SG})^+ \end{aligned}$$

Multiplying both sides by $\frac{L_{TC}}{\rho_{avg,core,0} (c_{p,avg,core})_0 (T_{avg,H} - T_{avg,C})_0 w_{avg,core,0}}$, we get

$$\begin{aligned} &\rho^+ c_p^+ \frac{\partial T^+}{\partial t^+} + \rho^+ c_p^+ w^+ \frac{\partial T^+}{\partial z^+} \\ &= \frac{k_{avg,core,0}}{\rho_{avg,core,0} (c_{p,avg,core})_0 w_{avg,core,0} L_{TC}} \rho^+ c_p^+ w^+ \frac{\partial T^+}{\partial z^+} \\ &+ \frac{(q'''_{core})_0 L_{TC}}{\rho_{avg,core,0} (c_{p,avg,core})_0 (T_{avg,H} - T_{avg,C})_0 w_{avg,core,0}} (q'''_{core})^+ \\ &+ \frac{(q'''_{SG})_0 L_{TC}}{\rho_{avg,core,0} (c_{p,avg,core})_0 (T_{avg,H} - T_{avg,C})_0 w_{avg,core,0}} (q'''_{SG})^+ \end{aligned}$$

Which gives us the following dimensionless Loop Energy Balance Equation,

$$\rho^+ c_p^+ \frac{\partial T^+}{\partial t^+} + \rho^+ c_p^+ w^+ \frac{\partial T^+}{\partial z^+} = \frac{1}{\Pi_{Pe,PCC}} k^+ \frac{\partial^2 T^+}{\partial z^+{}^2} + \Pi_{core,PCC} (q'''_{core})^+ + \Pi_{SG,PCC} (q'''_{SG})^+ \dots (7.2)$$

The characteristic ratios (Π -groups) appearing in these equations are defined by the following equations:

PCC Natural Circulation Geometry Ratio

$$(\Pi_{G,PCC})_R = \left[\sum_{i=1}^N \left(\frac{l_i a_{core}}{L_{TC} a_i} \right) \right]_R \dots (7.3)$$

PCC Natural Circulation Richardson Number Ratio

$$(\Pi_{Ri,PCC})_R = \left[\frac{g(\rho_{avg,C} - \rho_{avg,H})_0 L_{TC}}{\rho_{avg,core,0} W_{avg,core,0}^2} \right]_R \dots (7.4)$$

PCC Natural Circulation Resistance Number Ratio

$$(\Pi_{F,PCC})_R = \left[\sum_{i=1}^N \left[\left(\frac{fl}{d_h} + K \right)_i \left(\frac{\rho_{avg,core,0} a_{core}^2}{\rho_i a_i^2} \right) \right] \right]_R \dots (7.5)$$

PCC Natural Circulation Peclet Number Ratio

$$(\Pi_{Pe,PCC})_R = \left[\frac{\rho_{avg,core,0} (c_{p,avg,core})_0 W_{avg,core,0} L_{TC}}{k_{avg,core,0}} \right]_R \dots (7.6)$$

PCC Natural Circulation Core Power Ratio

$$(\Pi_{core,PCC})_R = \left[\frac{(q'''_{core})_0 L_{TC}}{\rho_{avg,core,0} (c_{p,avg,core})_0 W_{avg,core,0} (T_{avg,H} - T_{avg,C})_0} \right]_R \dots (7.7)$$

PCC Natural Circulation Steam Generator Heat Removal Ratio

$$(\Pi_{SG,PCC})_R = \left[\frac{(q'''_{SG})_0 L_{TC}}{\rho_{avg,core,0} (c_{p,avg,core})_0 W_{avg,core,0} (T_{avg,H} - T_{avg,C})_0} \right]_R \dots (7.8)$$

PCC Natural Circulation Time Scale Ratio

$$(t_{PCC})_R = \left[\frac{L_{TC}}{W_{avg,core,0}} \right]_R \dots \dots (7.9)$$

Initial values in the characteristic ratios (Π -groups) presented above occur at the beginning of natural circulation which is the initial time of the single-phase natural circulation phase of the PCC scenario. The similarity criteria and characteristic ratios (Π -groups) presented above should be set to unity wherever possible. Otherwise, scale ratios must be examined for distortion. In some instances, setting one ratio to unity is prioritized over another ratio. Thus, from a design point of view decision has to be made on which ratio to allow distortion.

7.1.2 Primary Loop Resistance

The dominant contributors to flow resistance in the MHTGR primary loop during the PCC event are the core and the steam generator (heat exchanger). For an inlet-outlet duct break, the flow resistance of the break will be a major contributor to natural circulation flow resistance across the break instead of the steam generator resistance. Considering helium expansion or compression effects to be negligible, the pressure drop across the core, heat exchanger and inlet-outlet duct break can be found using the following equations:

$$\Delta P_{PC,PCC,core} = \frac{\rho_{avg,c} W_{avg,core}^2}{2} \left(\frac{f_{core} L_{core}}{d_{h,core}} + K_{core} \right)$$

$$\Delta P_{PC,PCC,SG} = \frac{\rho_{avg,c} W_{avg,SG}^2}{2} \left(\frac{f_{SG} L_{SG}}{d_{h,SG}} + K_{SG} \right)$$

$$\Delta P_{PC,PCC,Brk} = \frac{\rho_{avg,H} W_{Brk}^2 K_{Brk}}{2}$$

The pressure drop across the core and the steam generator consists of frictional losses and form losses. For the break, the pressure drop consists of only form loss. The largest contributor to pressure drop in the prismatic block HTGR system is frictional pressure drop due to gas flow through the reactor core coolant channels. Balancing buoyancy and flow resistance under steady-state conditions, the pressure drop across the primary loop must scale as follows:

$$[\Delta P_{PC,PCC,core} + \Delta P_{PC,PCC,SG}]_R = [g(\rho_{avg,H} - \rho_{avg,H})L_{TC}]_R \dots \dots (7.10)$$

For the condition of fluid property similitude, we have:

$$[\Delta P_{PC,PCC,core} + \Delta P_{PC,PCC,SG}]_R = [L_{TC}]_R$$

In a reduced height facility, the designer can satisfy this criterion through the use of orifices to obtain the desired pressure drop around the loop. This balance between buoyancy and flow resistance under steady-state conditions can also be used when scaling natural circulation through a inlet-outlet duct break. In the case of a inlet-outlet duct break, the vessel length is used instead of the distance between thermal centers as the characteristic length. The pressure drop across the break loop must scale as follows:

$$[\Delta P_{PC,PCC,core} + \Delta P_{PC,PCC,Brk}]_R = [g(\rho_{avg,H} - \rho_{avg,H})L]_R \dots \dots (7.11)$$

For the condition of fluid property similitude, we have:

$$[\Delta P_{PC,PCC,core} + \Delta P_{PC,PCC,Brk}]_R = [L]_R$$

In a reduced height facility, the designer can satisfy this criterion through the use of orifices to obtain the desired pressure drop around the loop.

7.1.3 Heat Transfer

During natural circulation phase, convection becomes an important contributor to the transfer of heat in the system. The following equations can be used to describe the heat transfer during the natural circulation phase with and without a heat source:

$$\frac{k}{\alpha} \frac{\partial T}{\partial t} = \frac{1}{r} \frac{\partial}{\partial r} \left(kr \frac{\partial T}{\partial r} \right) + \frac{\partial}{\partial z} \left(k \frac{\partial T}{\partial z} \right) \dots (7.12)$$

$$\frac{k}{\alpha} \frac{\partial T}{\partial t} = \frac{1}{r} \frac{\partial}{\partial r} \left(kr \frac{\partial T}{\partial r} \right) + \frac{\partial}{\partial z} \left(k \frac{\partial T}{\partial z} \right) + q''_{core} \dots (7.13)$$

Rewriting the above equations in non-dimensionalized form:

$$\frac{k^+}{\alpha^+} \frac{\partial T^+}{\partial t^+} = \Pi_{Fo_d,NC} \frac{1}{r^+} \frac{\partial}{\partial r^+} \left(k^+ r^+ \frac{\partial T^+}{\partial r^+} \right) + \Pi_{Fo_L,NC} \frac{\partial}{\partial z^+} \left(k^+ \frac{\partial T^+}{\partial z^+} \right) \dots (7.14)$$

$$\begin{aligned} \frac{k^+}{\alpha^+} \frac{\partial T^+}{\partial t^+} = & \Pi_{Fo_d,NC} \frac{1}{r^+} \frac{\partial}{\partial r^+} \left(k^+ r^+ \frac{\partial T^+}{\partial r^+} \right) + \Pi_{Fo_L,NC} \frac{\partial}{\partial z^+} \left(k^+ \frac{\partial T^+}{\partial z^+} \right) \\ & + \Pi_{core,NC} \frac{\partial}{\partial z^+} (q''_{core})^+ \dots (7.15) \end{aligned}$$

Since helium flows through the channels in the prismatic block core, a convection boundary condition must be added to the flow channels in order to capture the effects of natural convection through the core region. The convection boundary condition is shown in following equation (7.16). In this equation, $T_{g,channel}$ represents the temperature of the coolant gas and $T_{wall,channel}$ represents the temperature of the core at the channel wall.

$$-k_{core} \frac{\partial T}{\partial r} \Big|_{wall,channel} = h_{wall,channel} (T_{wall,channel} - T_{g,channel}) \dots (7.16)$$

Non-dimensionalizing this boundary condition yields the following non-dimensionalized relation for the boundary condition in the core coolant channels. In equation (7.17), $d_{channel}$ represents the diameter of the core coolant channels.

$$\begin{aligned} -k_{core}^+ \frac{\partial T^+}{\partial r^+} \Big|_{wall,channel} &= \frac{(h_{wall,channel})_0}{(k_{core})_0} (T_{wall,channel} - T_{g,channel})^+ \\ &= \Pi_{Bi,NC,wall,channel} (T_{wall,channel} - T_{g,channel})^+ \dots (7.18) \end{aligned}$$

It is anticipated that the flow through the coolant channels during the natural circulation phase will be dominated by free convection. Equation (7.19) shows the Churchill-Chu correlation for natural convection on the surface of a vertical plate.

$$Nu_L = \left\{ 0.825 + \frac{0.387(Ra_L)^{1/6}}{\left[1 + \left(\frac{0.492}{Pr_g} \right)^{9/16} \right]^{8/27}} \right\} = \frac{h_{wall,channel} d_{channel}}{k_{g,channel}} \dots \dots (7.19)$$

From this correlation, it can be seen that the Nusselt number for the natural circulation heat transfer in the coolant channel is a function of the Rayleigh number and the Prandtl number.

The following are the similarity criteria for core and vessel heat transfer during the PCC event. The characteristic length scale for heat transfer in the core during the PCC event is based on the thermal center distance, L_{TC} , as shown in equation (7.9). As mentioned previously, the initial values in these ratios occur at the time of onset of natural circulation which is the initial time of the single-phase natural circulation phase of the PCC scenario.

Prismatic Core PCC Natural Circulation Radial Fourier Number Ratio

$$(\Pi_{Fo_d,PCC,core})_R = \left[\frac{(\alpha_{core})_0 L_{TC}}{w_{avg,core,0} d_{vessel}^2} \right]_R \dots \dots (7.20)$$

Prismatic Core PCC Natural Circulation Axial Fourier Number Ratio

$$(\Pi_{Fo_L,PCC,core})_R = \left[\frac{(\alpha_{core})_0 L_{TC}}{w_{avg,core,0} L^2} \right]_R \dots \dots (7.21)$$

Prismatic Core PCC Natural Circulation Core Power Ratio

$$\left(\Pi_{core,PCC}\right)_R = \left[\frac{(q'''_{core})_0(\alpha_{core})_0 L_{TC}}{(k_{core})_0 T_{core,max,0} W_{avg,core,0}} \right]_R \dots\dots (7.22)$$

Vessel PCC Natural Circulation Radial Fourier Number Ratio

$$\left(\Pi_{Fo_d,PCC,vessel}\right)_R = \left[\frac{(\alpha_{vessel})_0 L_{TC}}{W_{avg,core,0} d_{vessel}^2} \right]_R \dots\dots (7.23)$$

Vessel PCC Natural Circulation Axial Fourier Number Ratio

$$\left(\Pi_{Fo_L,PCC,vessel}\right)_R = \left[\frac{(\alpha_{vessel})_0 L_{TC}}{W_{avg,core,0} L^2} \right]_R \dots\dots (7.24)$$

Inner Vessel PCC Natural Circulation Modified Boltzmann Number Ratio

$$\left(\Pi_{Bo,PCC,vessel,i}\right)_R = \left[\frac{\sigma(\epsilon_{vessel,i})_0 T_{core,max,0}^3 d_{vessel}}{(k_{vessel})_0} \right]_R \dots\dots (7.25)$$

Prismatic Core Top PCC Natural Circulation Modified Boltzmann Number Ratio

$$\left(\Pi_{Bo,PCC,core,top}\right)_R = \left[\frac{\sigma(\epsilon_{core,top})_0 T_{core,max,0}^3 d_{vessel}}{(k_{core})_0} \right]_R \dots\dots (7.26)$$

Prismatic Core PCC Natural Circulation Channel Rayleigh Number Ratio

$$\left(\Pi_{Ra,channel,PCC}\right)_R = \left[\frac{g(\beta_{g,channel})_0 (T_{wall,channel} - T_{g,channel}) L^3}{(v_{g,channel} \alpha_{g,channel})_0} \right]_R \dots\dots (7.27)$$

Prismatic Core PCC Natural Circulation Channel Prandtl Number Ratio

$$\left(\Pi_{Pr,channel,PCC}\right)_R = \left[\frac{(v_{g,channel})_0}{(\alpha_{g,channel})_0} \right]_R \dots\dots (7.28)$$

Prismatic Core PCC Natural Circulation Channel Biot Number Ratio

$$\left(\Pi_{Bi,channel,PCC}\right)_R = \left[\frac{(h_{wall,channel})_0 d_{channel}}{(k_{core})_0} \right]_R \dots\dots (7.29)$$

7.2 Upper Plenum Mixing and Heat Transfer

During natural circulation, the amount of mixing that occurs as hot jets exit the top of the core is a candidate for high-temperature gas jets to impinge upon the inlet plenum vessel wall causing significant thermal stress. To effectively model this behavior both the gas jet mixing and the heat transfer to the inlet plenum vessel wall must be modeled accurately. Heat transfer occurs to the upper plenum vessel wall through the hot helium jets impinging on the inner vessel wall surface as well as thermal radiation from the top of the core. Helium is a non-participating medium when it comes to radiation heat transfer thus radiation does not affect the gas flow equations. (Bardet 2008) Thermal radiation only affects the boundary condition at the inlet plenum vessel wall. Figure-15 shows a jet mixing in an ambient environment.

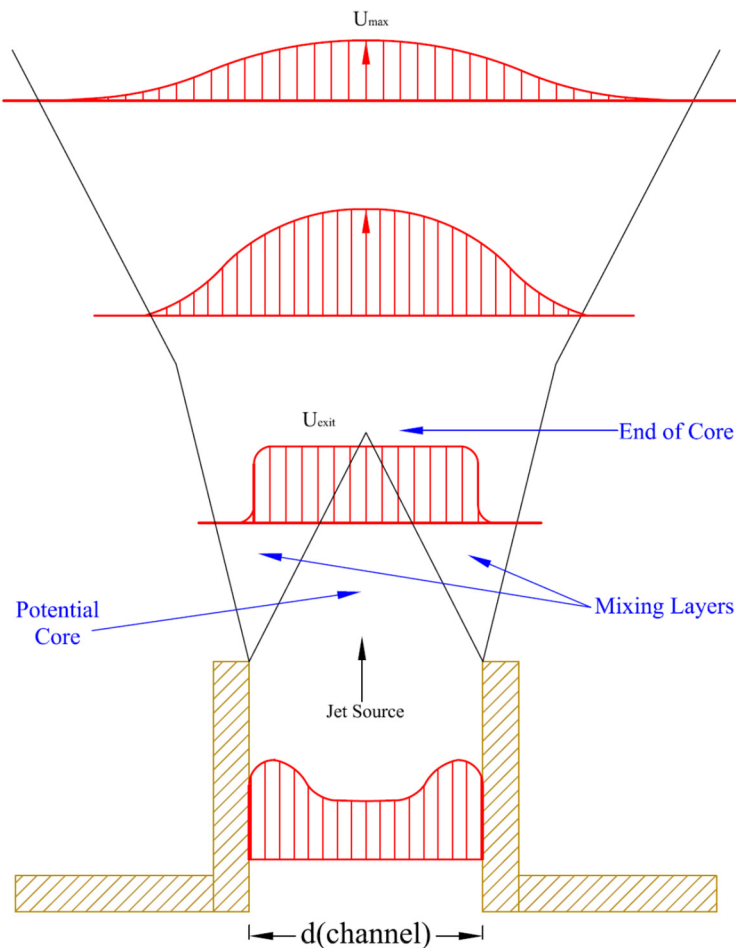


Figure 15: Jet mixing in Upper Plenum

Since the mixing of gas jets in the inlet plenum is a local phenomenon, a two-dimensional differential form of the conservation equations will be used. Azimuthal symmetry and an azimuthal velocity of zero will be assumed. It will also be assumed that the inlet plenum jets will be vertically oriented. Equations (7.30) and (7.31) show the differential mass and energy equations for a jet mixing in an ambient environment. Equations (7.32) and (7.33) show the general differential momentum equations for the r and z directions respectively. The pressure gradient term can be solved for by applying equation (7.34) to the quiescent region outside the jet. Substituting equation (7.34) into equation (7.33) modifies the momentum equation for modeling jet injection into an ambient environment as shown in equation (7.35).

$$\frac{\partial \rho}{\partial t} + \frac{1}{r} \frac{\partial}{\partial r} (\rho r u_r) + \frac{\partial}{\partial z} (\rho u_z) = 0 \dots \dots (7.30)$$

$$\rho c_p \frac{\partial T}{\partial t} + \rho c_p u_r \frac{\partial T}{\partial r} + \rho c_p u_z \frac{\partial T}{\partial z} = \frac{1}{r} \frac{\partial}{\partial r} \left(k r \frac{\partial T}{\partial r} \right) + \frac{\partial}{\partial z} \left(k \frac{\partial T}{\partial z} \right) = 0 \dots \dots (7.31)$$

$$\begin{aligned} & \rho \left(\frac{\partial u_r}{\partial t} + u_r \frac{\partial u_r}{\partial r} + u_z \frac{\partial u_r}{\partial z} \right) \\ &= \frac{1}{r} \frac{\partial}{\partial r} \left[\mu r \left(2 \frac{\partial u_r}{\partial r} - \frac{2}{3} \frac{1}{r} \frac{\partial}{\partial r} (r u_r) - \frac{2}{3} \frac{\partial u_z}{\partial z} \right) \right] + \frac{\partial}{\partial z} \left[\mu \left(\frac{\partial u_z}{\partial r} + \frac{\partial u_r}{\partial z} \right) \right] \\ & - \frac{\mu}{r} \left[2 \frac{u_r}{r} - \frac{2}{3} \frac{1}{r} \frac{\partial}{\partial r} (r u_r) - \frac{2}{3} \frac{\partial u_z}{\partial z} \right] - \frac{\partial p}{\partial r} \dots \dots (7.32) \end{aligned}$$

$$\begin{aligned} & \rho \left(\frac{\partial u_z}{\partial t} + u_r \frac{\partial u_z}{\partial r} + u_z \frac{\partial u_z}{\partial z} \right) \\ &= \frac{1}{r} \frac{\partial}{\partial r} \left[\mu r \left(\frac{\partial u_z}{\partial r} + \frac{\partial u_r}{\partial z} \right) \right] + \frac{\partial}{\partial z} \left[\mu \left(2 \frac{\partial u_z}{\partial z} - \frac{2}{3} \frac{1}{r} \frac{\partial}{\partial r} (r u_r) - \frac{2}{3} \frac{\partial u_z}{\partial z} \right) \right] - \frac{\partial p}{\partial z} \\ & + \rho g_z \dots \dots (7.33) \end{aligned}$$

$$\frac{\partial p}{\partial z} = -\rho_\infty g \dots \dots (7.34)$$

$$\begin{aligned} & \rho \left(\frac{\partial u_z}{\partial t} + u_r \frac{\partial u_z}{\partial r} + u_z \frac{\partial u_z}{\partial z} \right) \\ &= \frac{1}{r} \frac{\partial}{\partial r} \left[\mu r \left(\frac{\partial u_z}{\partial r} + \frac{\partial u_r}{\partial z} \right) \right] + \frac{\partial}{\partial z} \left[\mu \left(2 \frac{\partial u_z}{\partial z} - \frac{2}{3} \frac{1}{r} \frac{\partial}{\partial r} (r u_r) - \frac{2}{3} \frac{\partial u_z}{\partial z} \right) \right] \\ & + (\rho - \rho_\infty) g_z \dots \dots (7.35) \end{aligned}$$

The mass, momentum, and energy equations are normalized using the values at the boundary of the inlet plenum (top of the core and jet exit), the height of the inlet plenum (L_{IP}) and the diameter of the inlet jet (core flow channels) ($d_{channel}$). The following equations summarize the normalized variables that can be used with equations (7.30), (7.31), (7.32) and (7.35) to develop a non-dimensionalized set of equations for mass, momentum, and energy.

$$z^+ = \frac{z}{L_{TC}}$$

$$w^+ = \frac{w}{w_0} = \frac{wL}{w_0 D_{avg,core,0}}$$

$$k^+ = \frac{k}{k_{avg,core,0}}$$

$$\rho^+ = \frac{\rho}{\rho_{g,exit}}$$

$$\mu^+ = \frac{\mu}{\mu_{g,exit}}$$

$$(\Delta\rho)^+ = \frac{\rho - \rho_\infty}{\rho_{g,exit} - \rho_{w,IP}}$$

$$u_i^+ = \frac{u_i}{u_{g,exit}}$$

$$t^+ = \frac{t}{\tau} = \frac{t u_{g,exit}}{L_{IP}}$$

$$r^+ = \frac{r}{d_{channel}}$$

$$z^+ = \frac{z}{L_{IP}}$$

$$\alpha^+ = \frac{\alpha}{\alpha_{g,exit}}$$

The non-dimensionalized equations for mass, momentum and energy are shown below:

$$\frac{\partial \rho^+}{\partial t^+} + \left(\frac{L_{IP}}{d_{channel}} \right) \frac{1}{r^+} \frac{\partial}{\partial r^+} (\rho^+ r^+ u_r^+) + \frac{\partial}{\partial z^+} (\rho^+ u_z^+) = 0$$

$$\begin{aligned}
& \frac{\partial T^+}{\partial t^+} + \left(\frac{L_{IP}}{d_{channel}} \right) u_r^+ \frac{\partial T^+}{\partial r^+} + u_z^+ \frac{\partial T^+}{\partial z^+} \\
& = \left(\frac{\alpha_{g,exit}}{u_{g,exit} d_{channel}} \right) \left(\frac{L_{IP}}{d_{channel}} \right) \frac{1}{r^+} \frac{\partial}{\partial r^+} \left(k r^+ \frac{\partial T^+}{\partial r^+} \right) \\
& + \left(\frac{\alpha_{g,exit}}{u_{g,exit} L_{IP}} \right) \frac{\partial}{\partial z^+} \left(k \frac{\partial T^+}{\partial z^+} \right) \dots \dots 7.36
\end{aligned}$$

$$\begin{aligned}
& \rho^+ \left(\frac{\partial u_r^+}{\partial t^+} + \left(\frac{L_{IP}}{d_{channel}} \right) u_r^+ \frac{\partial u_r^+}{\partial r^+} + u_z^+ \frac{\partial u_r^+}{\partial z^+} \right) \\
& = \left(\frac{\mu_{g,exit}}{\rho_{g,exit} u_{g,exit} d_{channel}} \right) \frac{1}{r^+} \frac{\partial}{\partial r^+} \left[\mu^+ r^+ \left(\left(\frac{L_{IP}}{d_{channel}} \right) \left(2 \frac{\partial u_r^+}{\partial r^+} \right. \right. \right. \\
& \left. \left. \left. - \frac{2}{3} \frac{1}{r^+} \frac{\partial}{\partial r^+} (r^+ u_r^+) \right) - \frac{2}{3} \frac{\partial u_z^+}{\partial z^+} \right) \right] \\
& + \left(\frac{\mu_{g,exit}}{\rho_{g,exit} u_{g,exit} d_{channel}} \right) \frac{\partial}{\partial z^+} \left[\mu^+ \left(\frac{\partial u_z^+}{\partial r^+} + \left(\frac{d_{channel}}{L_{IP}} \right) \frac{\partial u_r^+}{\partial z^+} \right) \right] \\
& - \left(\frac{\mu_{g,exit}}{\rho_{g,exit} u_{g,exit} d_{channel}} \right) \frac{\mu^+}{r^+} \left[\left(\frac{L_{IP}}{d_{channel}} \right) \left(2 \frac{u_r^+}{r^+} - \frac{2}{3} \frac{1}{r^+} \frac{\partial}{\partial r^+} (r^+ u_r^+) \right) - \frac{2}{3} \frac{\partial u_z^+}{\partial z^+} \right] \\
& - \left(\frac{L_{IP}}{d_{channel}} \right) \frac{\partial p^+}{\partial r^+} \dots \dots 7.37
\end{aligned}$$

$$\begin{aligned}
& \rho^+ \left(\frac{\partial u_z^+}{\partial t^+} + \left(\frac{L_{IP}}{d_{channel}} \right) u_r^+ \frac{\partial u_z^+}{\partial r^+} + u_z^+ \frac{\partial u_z^+}{\partial z^+} \right) \\
& = \left(\frac{\mu_{g,exit}}{\rho_{g,exit} u_{g,exit} d_{channel}} \right) \frac{1}{r^+} \frac{\partial}{\partial r^+} \left[\mu^+ r^+ \left(\left(\frac{L_{IP}}{d_{channel}} \right) \frac{\partial u_z^+}{\partial r^+} + \frac{\partial u_r^+}{\partial z^+} \right) \right] \\
& + \left(\frac{\mu_{g,exit}}{\rho_{g,exit} u_{g,exit} d_{channel}} \right) \frac{\partial}{\partial z^+} \left[\mu^+ \left(\left(\frac{d_{channel}}{L_{IP}} \right) 2 \frac{\partial u_z^+}{\partial z^+} - \frac{2}{3} \frac{1}{r^+} \frac{\partial}{\partial r^+} (r^+ u_r^+) \right. \right. \\
& \left. \left. - \left(\frac{d_{channel}}{L_{IP}} \right) \frac{2}{3} \frac{\partial u_z^+}{\partial z^+} \right) \right] + \left(\frac{\rho_{g,exit} - \rho_{w,IP}}{\rho_{g,exit}} \right) \left(\frac{g L_{IP}}{u_{g,exit}^2} \right) (\rho - \rho_{\infty})^+ g \dots \dots 7.38
\end{aligned}$$

Equations (7.36), (7.37) and (7.38), can be re-written using the characteristic ratios for Peclet number, Reynolds number, and Froude number. The Peclet and Reynolds numbers here is

calculated using the channel diameter as the characteristic length dimension, while the Froude number is calculated using the height of the inlet plenum. The Froude number includes the ratio of density difference to density and is thus in the form of a densimetric Froude number.

$$\begin{aligned} \frac{\partial T^+}{\partial t^+} + \left(\frac{L_{IP}}{d_{channel}} \right) u_r^+ \frac{\partial T^+}{\partial r^+} + u_z^+ \frac{\partial T^+}{\partial z^+} \\ = \left(\frac{1}{\Pi_{Pe}} \right) \left(\frac{L_{IP}}{d_{channel}} \right) \frac{1}{r^+} \frac{\partial}{\partial r^+} \left(k r^+ \frac{\partial T^+}{\partial r^+} \right) + \left(\frac{1}{\Pi_{Pe}} \right) \left(\frac{d_{channel}}{L_{IP}} \right) \frac{\partial}{\partial z^+} \left(k \frac{\partial T^+}{\partial z^+} \right) \end{aligned}$$

$$\begin{aligned} \rho^+ \left(\frac{\partial u_r^+}{\partial t^+} + \left(\frac{L_{IP}}{d_{channel}} \right) u_r^+ \frac{\partial u_r^+}{\partial r^+} + u_z^+ \frac{\partial u_r^+}{\partial z^+} \right) \\ = \left(\frac{1}{\Pi_{Re}} \right) \frac{1}{r^+} \frac{\partial}{\partial r^+} \left[\mu^+ r^+ \left(\left(\frac{L_{IP}}{d_{channel}} \right) \left(2 \frac{\partial u_r^+}{\partial r^+} - \frac{2}{3} \frac{1}{r^+} \frac{\partial}{\partial r^+} (r^+ u_r^+) \right) - \frac{2}{3} \frac{\partial u_z^+}{\partial z^+} \right) \right] \\ + \left(\frac{1}{\Pi_{Re}} \right) \frac{\partial}{\partial z^+} \left[\mu^+ \left(\frac{\partial u_z^+}{\partial r^+} + \left(\frac{d_{channel}}{L_{IP}} \right) \frac{\partial u_r^+}{\partial z^+} \right) \right] \\ - \left(\frac{1}{\Pi_{Re}} \right) \frac{\mu^+}{r^+} \left[\left(\frac{L_{IP}}{d_{channel}} \right) \left(2 \frac{u_r^+}{r^+} - \frac{2}{3} \frac{1}{r^+} \frac{\partial}{\partial r^+} (r^+ u_r^+) \right) - \frac{2}{3} \frac{\partial u_z^+}{\partial z^+} \right] - \left(\frac{L_{IP}}{d_{channel}} \right) \frac{\partial p^+}{\partial r^+} \end{aligned}$$

$$\begin{aligned} \rho^+ \left(\frac{\partial u_z^+}{\partial t^+} + \left(\frac{L_{IP}}{d_{channel}} \right) u_r^+ \frac{\partial u_z^+}{\partial r^+} + u_z^+ \frac{\partial u_z^+}{\partial z^+} \right) \\ = \left(\frac{1}{\Pi_{Re}} \right) \frac{1}{r^+} \frac{\partial}{\partial r^+} \left[\mu^+ r^+ \left(\left(\frac{L_{IP}}{d_{channel}} \right) \frac{\partial u_z^+}{\partial r^+} + \frac{\partial u_r^+}{\partial z^+} \right) \right] \\ + \left(\frac{1}{\Pi_{Re}} \right) \frac{\partial}{\partial z^+} \left[\mu^+ \left(\left(\frac{d_{channel}}{L_{IP}} \right) 2 \frac{\partial u_z^+}{\partial z^+} - \frac{2}{3} \frac{1}{r^+} \frac{\partial}{\partial r^+} (r^+ u_r^+) - \left(\frac{d_{channel}}{L_{IP}} \right) \frac{2}{3} \frac{\partial u_z^+}{\partial z^+} \right) \right] \\ + \left(\frac{1}{\Pi_{Fr}^2} \right) (\rho - \rho_\infty)^+ g \end{aligned}$$

Based on above analysis, the characteristic time ratios for inlet plenum mixing can be summarized in the following relations:

PCC Inlet Plenum Mixing Geometry Ratio

$$\left(\Pi_{G,IPM}\right)_R = \left(\frac{L_{IP}}{d_{channel}}\right)_R \dots\dots (7.39)$$

PCC Inlet Plenum Mixing Peclet Number Ratio

$$\left(\Pi_{Pe,IPM}\right)_R = \left(\frac{u_{g,exit}d_{channel}}{\alpha_{g,exit}}\right)_R \dots\dots (7.40)$$

PCC Inlet Plenum Mixing Reynolds Number Ratio

$$\left(\Pi_{Re,IPM}\right)_R = \left(\frac{\rho_{g,exit}u_{g,exit}d_{channel}}{\mu_{g,exit}}\right)_R \dots\dots (7.41)$$

PCC Inlet Plenum Mixing Densimetric Froude Number Ratio

$$\left(\Pi_{Fr,IPM}\right)_R = \left(\frac{u_{g,exit}}{\sqrt{\left(\frac{\rho_{g,exit} - \rho_{w,IP}}{\rho_{g,exit}}\right)gL_{IP}}}\right)_R \dots\dots (7.42)$$

8. Scaling Analysis of Single Phase Forced Convection

During normal operations, the helium is circulated through the loop by means of a forced circulator. Heat transfer coefficients are typically much larger in a forced flow condition than normally found for natural circulation. For normal operations, the principal phenomenon of interest are the core temperature and outlet plenum flow distributions. A loop scaling analysis will be conducted in this section in order to determine the scaled boundary conditions required for examination of these phenomena.

8.1 Normal Operations Loop Scaling Analysis

During forced convection, the operator has the scope to select a mass flow rate through the operation of the circulator. The limits of mass flow rate are determined by the design and operational characteristics of the circulator. The operator also has the ability to select a core heat input up to the heater design limits. By controlling these parameters, the operator can set a temperature rise ratio between the prototype and model based on following equation. The assumption made here is that the system is at steady state and that the heat transfer through the core is dominated by the forced convection effects. Thus heat storage and heat loss effects can be taken as negligible.

$$(\Delta T_{NO,core})_R = \left(\frac{\dot{q}_{core}}{\dot{m}_{core} c_{p,avg,core}} \right)_R$$

Assuming temperature and gas concentration similarity yields the following relation between mass flow rate and core power.

$$(\dot{m}_{core})_R = (\dot{q}_{core})_R$$

8.2 Heat Transfer

Transient heat transfer scaling ratios have been developed for natural circulation in the previous section. Steady-state governing equations for heat transfer through regions with and without a heat source are shown in the following equations (8.1) and (8.2).

$$\frac{1}{r} \frac{\partial}{\partial r} \left(kr \frac{\partial T}{\partial r} \right) + \frac{\partial}{\partial z} \left(k \frac{\partial T}{\partial z} \right) + q'''_{core} = 0 \dots \dots (8.1)$$

$$\frac{1}{r} \frac{\partial}{\partial r} \left(kr \frac{\partial T}{\partial r} \right) + \frac{\partial}{\partial z} \left(k \frac{\partial T}{\partial z} \right) = 0 \dots \dots (8.2)$$

Using dimensionless parameters along with the dimensionless temperature from equation (8.3), yields the non-dimensional forms of equations (8.1) and (8.2).

$$T^+ = \frac{T}{T_{core,max}} \dots \dots (8.3)$$

$$\frac{1}{r^+} \frac{\partial}{\partial r^+} \left(k^+ r^+ \frac{\partial T^+}{\partial r^+} \right) + \left(\frac{d_{vessel}^2}{L^2} \right) \frac{\partial}{\partial z^+} \left(k^+ \frac{\partial T^+}{\partial z^+} \right) + \frac{q_{core}''' d_{vessel}^2}{k_{core} T_{core,max}} (q_{core}''')^+ = 0$$

$$\frac{1}{r^+} \frac{\partial}{\partial r^+} \left(k^+ r^+ \frac{\partial T^+}{\partial r^+} \right) + \left(\frac{d_{vessel}^2}{L^2} \right) \frac{\partial}{\partial z^+} \left(k^+ \frac{\partial T^+}{\partial z^+} \right) = 0$$

$$\frac{1}{r^+} \frac{\partial}{\partial r^+} \left(k^+ r^+ \frac{\partial T^+}{\partial r^+} \right) + (\Pi_{G,NO})_R \frac{\partial}{\partial z^+} \left(k^+ \frac{\partial T^+}{\partial z^+} \right) + (\Pi_{core,NO})_R (q_{core}''')^+ = 0 \dots (8.4)$$

$$\frac{1}{r^+} \frac{\partial}{\partial r^+} \left(k^+ r^+ \frac{\partial T^+}{\partial r^+} \right) + (\Pi_{G,NO})_R \frac{\partial}{\partial z^+} \left(k^+ \frac{\partial T^+}{\partial z^+} \right) = 0 \dots \dots (8.5)$$

The radiation and convection boundary conditions developed in previous section can be applied to the boundaries of the forced convection problem. The following equation (8.6) shows the Dittus-Boelter Nusselt number correlation used to determine the heat transfer coefficient during forced convection.

$$Nu_D = 0.023 Re_D^{0.8} Pr_g^{0.4} = \frac{h_{wall,channel} d_{channel}}{k_{g,channel}} \dots \dots (8.6)$$

Based on this analysis, the following are the similarity criteria for core and vessel heat transfer during normal operations. If possible the ratio should be set to unity. Otherwise, scale ratios must be examined for distortion. In some instances, setting a ratio to one precludes setting another to one and thus choices as to which ratio to allow distortion in must be made.

Vessel Normal Operations Geometry Ratio

$$(\Pi_{G,NO})_R = \left[\frac{d_{vessel}^2}{L^2} \right]_R \dots \dots (8.7)$$

Prismatic Core Normal Operations Core Power Ratio

$$(\Pi_{core,NO})_R = \left[\frac{q'''_{core} d_{vessel}^2}{k_{core} T_{core,max}} \right]_R \dots \dots (8.8)$$

Prismatic Core Normal Operations Channel Reynolds Number Ratio

$$(\Pi_{Re,channel,NO})_R = \left[\frac{\rho_{g,channel} u_{avg,channel} d_{channel}}{\mu_{g,channel}} \right]_R \dots \dots (8.9)$$

Prismatic Core Normal Operations Channel Prandtl Number Ratio

$$(\Pi_{Pr,channel,NO})_R = \left[\frac{v_{g,channel}}{\alpha_{g,channel}} \right]_R \dots \dots (8.10)$$

Upcomer Normal Operations Channel Reynolds Number Ratio

$$(\Pi_{Re,upcomer,NO})_R = \left[\frac{\rho_{g,upcomer} u_{avg,upcomer} d_{upcomer}}{\mu_{g,upcomer}} \right]_R \dots \dots (8.11)$$

Upcomer Operations Channel Prandtl Number Ratio

$$(\Pi_{Pr,upcomer,NO})_R = \left[\frac{v_{g,upcomer}}{\alpha_{g,upcomer}} \right]_R \dots \dots (8.12)$$

8.3 Lower Plenum Mixing

During normal operations, the mixing of hot jets determines the temperature of gas jets impinging upon the outlet hot duct and components located in lower plenum as they exit the bottom of the prismatic core. The amount of mixing that occurs in the outlet plenum will depend largely on the geometry of the support structures in the outlet plenum and thus any geometric differences will impact the amount and character of gas jet mixing in the lower plenum. Figure-16 shows an outlet plenum in the MHTGR. The outlet plenum posts are arranged approximately perpendicular to the general direction of gas flow out of the outlet plenum to the outlet cross duct.

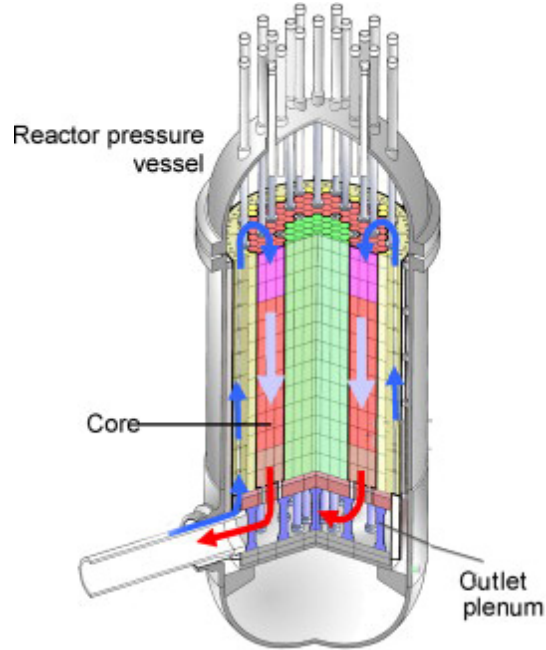


Figure 16: MHTGR Outlet Plenum

For the development of governing equations to describe jet mixing in the lower plenum, we will assume that:

- (1) the flow is isothermal,
- (2) jets move primarily in the radial and azimuthal directions (thus neglecting axial velocity and gradients), and
- (3) buoyancy forces can be neglected, the following

equations of motion can be developed to describe jet mixing in the outlet plenum.

$$\frac{\partial \rho}{\partial t} = \frac{1}{r} \frac{\partial}{\partial r} (\rho r u_r) + \frac{1}{r} \frac{\partial}{\partial \theta} (\rho u_\theta)$$

$$\rho \left(\frac{\partial u_r}{\partial t} + u_r \frac{\partial u_r}{\partial r} + \frac{u_\theta}{r} \frac{\partial u_r}{\partial \theta} - \frac{u_\theta^2}{r} \right)$$

$$= \frac{1}{r} \frac{\partial}{\partial r} \left[\mu r \left(2 \frac{\partial u_r}{\partial r} - \frac{2}{3r} \left(\frac{\partial}{\partial r} (r u_r) + \frac{\partial u_\theta}{\partial \theta} \right) \right) \right] + \frac{1}{r} \frac{\partial}{\partial \theta} \left[\mu \left(r \frac{\partial}{\partial r} \left(\frac{u_\theta}{r} \right) + \frac{1}{r} \frac{\partial u_r}{\partial \theta} \right) \right]$$

$$- \frac{\mu}{r^2} \left[\frac{4}{3} \frac{\partial u_\theta}{\partial \theta} + 2u_r - \frac{2}{3} \frac{\partial}{\partial r} (r u_r) \right] - \frac{\partial p}{\partial r}$$

$$\begin{aligned}
& \rho \left(\frac{\partial u_\theta}{\partial t} + u_r \frac{\partial u_\theta}{\partial r} + \frac{u_\theta}{r} \frac{\partial u_\theta}{\partial \theta} - \frac{u_r u_\theta}{r} \right) \\
&= \frac{1}{r^2} \frac{\partial}{\partial r} \left[\mu r^2 \left(r \frac{\partial}{\partial r} \left(\frac{u_\theta}{r} \right) + \frac{1}{r} \frac{\partial u_r}{\partial \theta} \right) \right] + \frac{1}{r} \frac{\partial}{\partial \theta} \left[\frac{\mu}{r} \left(\frac{4}{3} \frac{\partial u_\theta}{\partial \theta} + 2u_r - \frac{2}{3} \frac{\partial}{\partial r} (ru_r) \right) \right] \\
&\quad - \frac{1}{r} \frac{\partial p}{\partial r}
\end{aligned}$$

The continuity and momentum equations are normalized using the values at the boundary of the outlet plenum (outlet plenum roof and jet exit) and the diameter of the outlet plenum post (d_{post}). The following equations summarize the normalized variables will be used to develop a non-dimensionalized set of equations for continuity and momentum.

$$\rho^+ = \frac{\rho}{\rho_{g,exit}}$$

$$\mu^+ = \frac{\mu}{\mu_{g,exit}}$$

$$u_i^+ = \frac{u_i}{u_{g,exit}}$$

$$t^+ = \frac{t}{\tau} = \frac{tu_{g,exit}}{d_{post}}$$

$$r^+ = \frac{r}{d_{post}}$$

$$p^+ = \frac{p}{\rho_{g,exit} u_{g,exit}^2}$$

The non-dimensionalized equations for continuity and momentum are shown below as equations (8.13), (8.14) and (8.15).

$$\frac{\partial \rho^+}{\partial t^+} = \frac{1}{r^+} \frac{\partial}{\partial r^+} (\rho^+ r^+ u_r^+) + \frac{1}{r^+} \frac{\partial}{\partial \theta} (\rho^+ u_\theta^+) \dots \dots (8.13)$$

$$\begin{aligned}
& \rho^+ \left(\frac{\partial u_r^+}{\partial t^+} + u_r \frac{\partial u_r^+}{\partial r^+} + \frac{u_\theta^+}{r^+} \frac{\partial u_r^+}{\partial \theta} - \frac{u_\theta^+ u_\theta^+}{r^+} \right) \\
&= \left(\frac{\mu_{g,exit}}{\rho_{g,exit} u_{g,exit} d_{post}} \right) \frac{1}{r^+} \frac{\partial}{\partial r^+} \left[\mu r^+ \left(2 \frac{\partial u_r^+}{\partial r^+} - \frac{2}{3r^+} \left(\frac{\partial}{\partial r^+} (r^+ u_r^+) + \frac{\partial u_\theta^+}{\partial \theta} \right) \right) \right] \\
&+ \left(\frac{\mu_{g,exit}}{\rho_{g,exit} u_{g,exit} d_{post}} \right) \frac{1}{r^+} \frac{\partial}{\partial \theta} \left[\mu^+ \left(r^+ \frac{\partial}{\partial r^+} \left(\frac{u_\theta^+}{r^+} \right) + \frac{1}{r^+} \frac{\partial u_r^+}{\partial \theta} \right) \right] \\
&- \left(\frac{\mu_{g,exit}}{\rho_{g,exit} u_{g,exit} d_{post}} \right) \frac{\mu^+}{r^+ r^+} \left[\frac{4}{3} \frac{\partial u_\theta^+}{\partial \theta} + 2u_r^+ - \frac{2}{3} \frac{\partial}{\partial r^+} (r^+ u_r^+) \right] - \frac{\partial p^+}{\partial r^+} \dots \dots (8.14)
\end{aligned}$$

$$\begin{aligned}
& \rho^+ \left(\frac{\partial u_\theta^+}{\partial t} + u_r \frac{\partial u_\theta^+}{\partial r} + \frac{u_\theta^+}{r} \frac{\partial u_\theta^+}{\partial \theta} - \frac{u_r^+ u_\theta^+}{r} \right) \\
&= \left(\frac{\mu_{g,exit}}{\rho_{g,exit} u_{g,exit} d_{post}} \right) \frac{1}{r^+ r^+} \frac{\partial}{\partial r^+} \left[\mu^+ r^+ r^+ \left(r^+ \frac{\partial}{\partial r^+} \left(\frac{u_\theta^+}{r^+} \right) + \frac{1}{r^+} \frac{\partial u_r^+}{\partial \theta} \right) \right] \\
&+ \left(\frac{\mu_{g,exit}}{\rho_{g,exit} u_{g,exit} d_{post}} \right) \frac{1}{r^+} \frac{\partial}{\partial \theta} \left[\frac{\mu^+}{r^+} \left(\frac{4}{3} \frac{\partial u_\theta^+}{\partial \theta} + 2u_r^+ - \frac{2}{3} \frac{\partial}{\partial r^+} (r^+ u_r^+) \right) \right] \\
&- \frac{1}{r^+} \frac{\partial p^+}{\partial r^+} \dots \dots (8.15)
\end{aligned}$$

From above analysis we see that the Reynolds numbers are the main characteristic time ratios for outlet plenum mixing.

Normal Operations Outlet Plenum Mixing Reynolds Number Ratio

$$(\Pi_{Re,OPM})_R = \left[\frac{\rho_{g,exit} u_{g,exit} d_{post}}{\mu_{g,exit}} \right]_R \dots \dots (8.16)$$

9. Distortion Analysis

In the previous section, we have yielded a set of similarity criteria that can be used to determine the dimensions and operating conditions for reduced-scale facilities. These similarity criteria are expressed in terms of dimensionless ratios of the model to prototype fluid, material, and geometric properties. If the ratios deviate from unity, then we must calculate distortion in order to appropriately incorporate the validation data collected from the experimental facilities into the advanced numerical tools.

9.1 Pressurized Conduction Cooldown Event Scaling Evaluation

CCNY has one single cooling channel and single bypass compared to the 516 flow channels of HTTF. Also, the CCNY design doesn't include any reflectors which might further affect the heat transfer phenomenon. The surface area to volume ratio of the CCNY facility is higher than that of HTTF. This will result into excess heat transfer to the surroundings.

HTTF uses prismatic graphite blocks as a moderator in its core. This huge chunk of graphite is very effective to dissipate heat from the core. But, the CCNY facility does not have such heat dissipation mechanism this will likely result in lower heat transfer to outside.

9.1.1 Natural Circulation

The set of scaling ratios for PCC natural circulation are identified in sections 7.1, 7.2, and 7.3. In this section, we will examine the scaling design requirements for the natural circulation phase of the PCC event. The following discussion will assume that the initial conditions for the natural circulation phase have been set by the facility operators and thus temperature similarity will be achieved.

9.1.1.1 Natural Circulation Geometry Ratio

The natural circulation geometry ratio is shown in equation (7.3). In order to preserve this ratio at unity, all component lengths of CCNY facility must scale the same as the length between the thermal centers of the core and the heat exchanger. Also, all component cross-sectional areas must scale as the cross-sectional area of the core. The geometry scaling of the core has the highest significance since this is the region with greatest flow resistance. Table-9.1 shows the

calculation of the natural circulation geometry ratio of HTTF to CCNY for the heated core region for the PCC event.

9.1.1.2 Natural Circulation Richardson Number Ratio

The Richardson Number for PCC natural circulation is given by equation (7.4). In the case of the inlet-outlet duct break, with flow through the steam generator stagnant, the core flow velocity ratio caused by flow through the break is given by equation (9.1).

$$(w_{avg,core})_R = (q'''_{core,0} L^2)_R^{\frac{1}{3}} = (L)_R^{\frac{1}{2}} \dots (9.1)$$

The velocity ratio can be determined using the following equations (9.2) and (9.3).

$$w_{avg,core} = \frac{\beta_{g,vessel} g \dot{q}_{core} L}{\rho_{avg,core} a_{core} c_{p,avg,core} \Pi_{F,NC}} \dots (9.2)$$

$$(q'''_{core,0})_R = \left(\frac{w_{avg,core}}{L} \right)_R \dots (9.3)$$

The natural circulation Richardson number ratio for the break loop can be calculated using the above core velocity ratio, equation (7.4) and the vessel height ratio (L). The calculation is shown in equation (9.4) below.

$$(\Pi_{Ri,NC})_R = \left(\frac{L}{w_{avg,core}^2} \right)_R \dots (9.4)$$

9.1.1.3 Natural Circulation Resistance Number Ratio

During natural circulation phenomena, the buoyancy force will drive natural circulation through the loop. For steady-state conditions following initiation of the PCC event, equation (7.10) shows the pressure drop requirements across the core and steam generator.

In the case of the inlet-outlet duct break, with flow through the heat exchanger becoming stagnant, the pressure drop across the core and break is shown in equation (7.11). We can assume temperature and gas concentration similarity, but not pressure similarity during the PCC event. Using these assumptions, the following equation for the pressure drop ratio will lead to resistance number similarity. The scaled pressure drop can be achieved in the CCNY facility through the use of orifices or geometric modifications.

$$\Delta P_{PC,PCC,core} + \Delta P_{PC,PCC,Brk} = [P_0 L]_0$$

9.1.1.4 Natural Circulation Peclet Number Ratio

The natural circulation Peclet number ratio for the PCC is calculated using equation (7.6). For stagnant loop flow, this ratio will be equal to unity. For flow through the inlet-outlet duct break, with temperature and gas concentration similarity, the ratio is calculated using the following equation. Thermal conductivity and specific heat are considered to be independent of pressure.

$$(\Pi_{Pe,PCC,IODB})_R = [P_0 w_{avg,core,0} L]_R = [P_0 L^{2/3}]_R$$

9.1.1.5 Natural Circulation Core Power Ratio

The natural circulation core power ratio for the PCC is calculated using equation (7.7). For stagnant loop flow, this ratio will be equal to unity. For flow through the inlet-outlet duct break, with temperature and gas concentration similarity, the ratio is calculated using the following equation.

$$(q'''_{core})_R = \left(\frac{P_0}{L^{1/2}} \right)_R$$

Scaled core power can be determined using the scaled core power density and scaled volume as shown in equation (8-35).

$$(\dot{q}_{core,0})_R = (q'''_{core}, V)_R = \left(P_0 L^{1/2} d_{vessel}^2 \right)_R \dots (9.5)$$

9.1.1.5 Natural Circulation Acceleration Parameter

When temperature inside the cooling channel increases, density of helium decreases. Thus, the velocity increases in the streamwise direction that corresponds to a favorable streamwise pressure gradient, which is known to stabilize laminar boundary layers. For a turbulent flow, the acceleration would tend to stabilize bursting from the important viscous layer and thereby reduce turbulent transport [Corino and Brodkey, 1969]. With sufficiently large acceleration, flow "laminarization" may take place inside the cooling channel where flows expected to be turbulent; show heat transfer parameters as low as in laminar flows [Bankston, 1970]. A measure of this phenomenon is an acceleration parameter K_v . For the cooling channel K_v is defined as

$$K_v \approx 4q^+ / Re_D \dots (9.6)$$

Moretti and Kays [1965] suggested that for $K_v < 3 \times 10^{-6}$ the flow would remain turbulent while for higher values it is likely to laminarize, giving a substantial reduction in heat transfer parameters.

9.1.1.6 Natural Circulation Buoyancy Parameter

Buoyancy force affects the convective heat transfer phenomena inside the cooling channels. Heat transfer may increase or decrease based on the direction of flow (direction of body force in relation to axial temperature and pressure gradients), and the nature of the flow (i.e. turbulent or laminar flow). In case of turbulent flow, the convective heat transfer can become inhibited in upflow while in downflow it could be enhanced; these observations are opposite to those for laminar flow [Jackson, Cotton and Axcell, 1989].

Table 1: Effects of buoyancy on convective heat transfer

Flow	Direction	Convective Heat Transfer
Laminar	Upflow	Enhanced
	Downflow	Degraded
Turbulent	Upflow	Degraded
	Downflow	Enhanced

With a specified wall heat flux, the Grashof number is usually defined as

$$Gr^* = g\beta q''_{wall} D_h^4 / (k\tau^2)$$

Applying the following Dittus-Boelter correlation for gases

$$Nu_D = 0.021 Re_D^{0.8} Pr_g^{0.4}$$

and the Blasius friction correlation, Jackson [Mikielewicz et al., 2002] developed an approximate criterion for fully-developed flow in circular channels. Buoyancy influences in fully-established flow in terms of a buoyancy parameter can be written as

$$Bo^* = Gr^* / (Re_D^{3.425} Pr^{0.8}) \dots (9.7)$$

The semi-empirical model of Jackson and Hall [Jackson, Cotton and Axcell, eqn. 11, 1989] demonstrate that the value of $Bo^* \approx 6 \times 10^{-7}$ provides a reasonable order-of-magnitude estimate of the buoyancy threshold for a vertical circular cooling channel.

9.1.1.7 Natural Circulation Steam Generator Heat Removal Ratio

The natural circulation steam generator heat removal ratio for the PCC is calculated using equation (7.8). For stagnant loop flow, this ratio will be equal to unity. For flow through the inlet-outlet duct break, this ratio will also be equal to unity since the loop through the heat exchanger will be stagnant in both the CCNY facility and HTTF.

9.1.1.8 Natural Circulation Time Scale Ratio

For PCC natural circulation, the time scale ratio can be determined using equation (7.9). The time scale ratio is only meaningful for inlet-outlet break flow through the break.

Table 2: Characteristic ratios and Flow parameters for PCC natural circulation upper plenum jet impingement (TAMU, MHTGR)

Characteristic Ratio/ Parameter	Equation	Ratio (TAMU /MHTGR)	Distortion
$(\Pi_{G,PCC})_R$	(7.3)	1.1	0.0
$(\Pi_{RI,PCC})_R$	(7.4)	1.1	0.0
$(\Pi_{core,PCC})_R$	(7.7)	1.1	0.0
K_v	(9.6)	1.1	0.0
Bo^*	(9.7)	1.1	0.0

9.1.2 PCC Upper Plenum Mixing and Heat Transfer

The inlet plenum mixing scaling ratios are developed in section 7.2. Table-3 shows the calculation of this ratios for the PCC event.

Table 3: Characteristic ratios for PCC Upper plenum mixing (TAMU, MHTGR)

Characteristic Ratio/ Parameter	Equation	Ratio (TAMU /MHTGR)	Distortion
$(\Pi_{G,IPM})_R$	(7.39)	1.1	0.0
$(\Pi_{Pe,IPM})_R$	(7.40)	1.1	0.0
$(\Pi_{Re,IPM})_R$	(7.41)	1.1	0.0
$(\Pi_{Fr,IPM})_R$	(7.42)	1.1	0.0

Table 4: Characteristic ratios for PCC natural circulation heat transfer (CCNY, HTTF)

Characteristic Ratio	Equation	Ratio (CCNY /HTTF)	Distortion
$(\Pi_{G,PCC})_R$	(7.3)	1:1	0.0
$(\Pi_{Ri,PCC})_R$	(7.4)	1:1	0.0
$(\Pi_{Pe,PCC})_R$	(7.6)	1:1	0.0
$(\Pi_{core,PCC})_R$	(7.7)	1:1	0.0
$(\Pi_{Pr,channel,PCC})_R$	(7.28)	1:1	0.0
K_v	(9.6)	1.1	0.0
Bo^*	(9.7)	1.1	0.0

9.2 Single Phase Forced Convection Scaling Evaluation

Some of the separate effect test facilities use different working fluid other than helium. For example the MIR facility uses mineral oil as working fluid in order to match the refraction index. Inside MIR facility quartz posts are employed which have the same refractive index as the mineral oil. In this way, the solid disappears optically (and therefore has no influence on the laser beams) but maintains its full mechanical influence on the flow. With a transparent model of different refractive index than the working fluid, the light rays of optical measuring instruments can be refracted in such a manner that measurements are either impossible or require extensive, difficult calibrations.

Mineral oil has different flow characteristics than helium which is the working fluid of MHTGR. Furthermore, the MIR facility conducts its operation at room temperature, whereas the helium exit-temperature at the MHTGR is 697°C. Such factors are likely to affect mixing criteria and hot spots formation in the lower plenum.

9.2.1 Normal Operations

The set of scaling ratios for normal operations are identified in section 8.2. In this section, we will examine the scaling design requirements for normal operations.

9.2.1.1 Vessel Normal Operations Geometry Ratio

The normal operations geometry ratio is shown in equation (8.7) and is calculated in table 9.3.

9.2.1.2 Normal Operations Core Power Ratio

The normal operations core power ratio is shown in equation (8.8). Assuming temperature similarity, for equation (8.8) to be equal to unity, the following core power ratio must be achieved.

$$(\dot{q}_{core,0})_R = (q'''_{core}, V)_R = \left(\frac{k_{core,radial} d_{vessel}^2 L}{d_{vessel}^2} \right)_R = (k_{core,radial} L)_R \cdots (9.8)$$

9.2.2 Outlet Plenum Mixing

The characteristic time ratio of interest during outlet plenum mixing is the Reynolds number ratio calculated using equation (8.16).

Table 5: Characteristic ratios for normal operations

Characteristic Ratio	Equation	Ratio (MIR/MHTGR)	Distortion
$(\Pi_{G,NO})_R$	(8.7)	1:1	0.0
$(\Pi_{core,NO})_R$	(8.8)	1:1	0.0
$(\Pi_{Re,channel,NO})_R$	(8.9)	1:1	0.0
$(\Pi_{Re,upcomer,NO})_R$	(8.11)	1:1	0.0
$(\Pi_{Re,OPM})_R$	(8.16)	1:1	0.0

10. Using Vintage Data to Validate Modern Numerical Methods: Data Superposition

Over the years a huge quantity of data have been recorded for validating numerical models written to analyze the thermal-hydraulic behavior of reactors—particularly light water reactors. These data are especially prevalent for French/Westinghouse¹-type pressurized water reactors. Much of the data described above, which were collected at numerous experimental facilities around the world, were vintage data² generated to validate one-dimensional numeric models. However some data were collected to map out two- and three-dimensional flow behavior in great detail for specific regions during key accident scenarios.

Because the above experiments designed to address potential issues, to study specific phenomenon, and to study the interactions between multiple phenomena share common geometries and boundary conditions, there is the potential to use an ensemble of data sets from related experiments even including different experimental facilities to produce a more comprehensive picture of fluid/heat transfer behavior than would be otherwise possible when considering only individual experiments. By using data superposition techniques, an ensemble of data sets may be combined and form a more comprehensive validation data set useful for validating modern numerical models.

10.1 Conceptual Approach

The degree of success for any attempt to superposition data from one facility to another is dependent on several key assumptions:

1. The experimental facilities were designed using the same scaling methodology.
2. The experimental facilities:
 - a. Address the same scenario with the same boundary and initial conditions—thus the transient progression in the facilities is the same.

¹ Including also Combustion Engineering designs.

² Vintage data are defined as measurements specific to large control volumes such as temperatures or pressures of large regions in a facility. High-fidelity data are detailed data designed to study the turbulent flow structure in a region of a system; typical diagnostics for high-fidelity data are particle-image velocimeters.

- b. Use the same working fluid,
- c. Have nearly identical thermodynamic conditions,
- d. Have matching conditions at their component boundaries, e.g., at the boundary between the core and either an inlet or outlet plenum.

If these conditions are not achieved, then data interchange between experimental facilities is reduced and may focus primarily on matching key non-dimensional numbers linked directly to the figures-of-merit used to design and scale the facilities of interest.

The first attempt to apply the above techniques was aimed at bringing together the large break loss-of-coolant accident data from the LOFT integral facility (1/60-scale) with the full-scale separate-effects full-scale facilities: Upper Plenum Test Facility constructed in Germany and the Japanese facilities: Cylindrical Core Test Facility and Slab Core Test Facility—since this group of facilities all meet the key assumptions listed above. However complete data sets from these facilities proved to be no longer available.

The process of linking data sets for the very high temperature reactor is described in the following paragraphs. The VHTR experimental facilities lend themselves to data superposition since the experimental facilities used to generate validation data were all scaled using the two-tiered hierarchical scaling methodology and were aimed at generating data for the same scenarios. However, the VHTR facilities did not: (a) use the same working fluids, (b) have the same thermodynamic conditions, (d) and thus did not have matching conditions at component boundaries. Nevertheless, a degree of data superposition may be achieved by focusing on matching non-dimensional numbers relevant to the figures-of-merit. In this case the “vintage data” are recorded in the integral facility—the High Temperature Test Facility (HTTF) and the Core Cooling Facility at the City College of New York. High-fidelity data are recorded in the separate-effects facilities such as the Texas A&M (TAMU) Upper Plenum Mixing Facility and the INL Matched-Index-of-Refractive-Index (MIR) facility. Here the high-fidelity data obtained in the TAMU Upper Plenum Mixing Facility will be used as an example to study mixing in the upper plenum of a VHTR.

10.1.1 Background

Following a loss-of-offsite power the circulators, in a Very High Temperature Gas-Cooled Reactor (VHTR), quickly coast-down in conjunction with insertion of the control rods.

Thereafter, if the VHTR: (a) does not have a leak in the primary pressure boundary: the scenario is commonly known as a pressurized conduction cooldown (PCC) or (b) does have a leak in the primary pressure boundary: the scenario is commonly known as a depressurized conduction cooldown (DCC).

In either case the core flow, normally downward-oriented under operational conditions, reverses and flows upward. The core flow rate is governed by the heat transferred to the gases in the core in combination with the core geometry, frictional pressure loss characteristics, and the relevant material properties. The core flow in either situation is density-gradient dominated in the core coolant channels. The gases flow from the core region into the upper plenum where it moves upward to either impinge on the upper hemisphere (if the flow rate is momentum-driven stemming from relatively large heat fluxes and thus a jet) or the gases flow gently upward to merge with gases in the upper regions of the plenum (if the flow rate remains density-gradient driven in the plenum and thus a plume). In some situations the flow may emerge from the core coolant channels as a jet and then evolve to a plume, prior to reaching the nearest structure, as it moves upward.

10.1.2 Issue

For the PCC and DCC scenarios the heat transfer from the hot jets or plumes to the hemispherical VHTR vessel structure and internals is a figure-of-merit from both an operational perspective and a safety perspective precisely because the global gas temperature in the vicinity of the upper plenum ceiling must not exceed (a) specified temperature limits (probably unlikely since Generation IV VHTRs are designed with sufficient margin to prevent limiting temperatures from occurring) and also (b) specified local material temperature gradients (much more probable since there are no design accommodations to provide for uniform gas temperature distributions) leading to material cracking.

Whether the upward moving flow is in the form of a jet or a plume results in a significant difference regarding the heat transfer behavior between the upper plenum gases and the upper hemisphere of the VHTR vessel. The presence of just plumes in the upper plenum will lead to the formation of a warm or hot stratified gas layer adjacent to the upper plenum ceiling that will distribute the gas layer temperature in a relatively uniform fashion leading to relatively uniform heating of the ceiling surface: thus this scenario leads to relatively uniform temperatures and minimizes thermal gradients in the upper hemisphere material. The presence of jets that are sufficiently vigorous to move through the stratified gas layer adjacent to the ceiling of the VHTR upper hemisphere and impinge on the material of the hemisphere leads to the scenario with a potential cooling issue: local high heat transfer rates with undesirable thermal gradients in the material sufficient to cause cracking.

10.2 Projected Reynolds Number and Gas Temperatures in VHTR Upper Plenum: PCC and DCC Scenarios

To investigate the likelihood of whether jets or plumes are present in the VHTR upper plenum during the PCC and DCC scenarios together with the gas temperatures of these jets/plumes—we make use of RELAP5 calculations performed to investigate the MHTGR behavior for these scenarios.

10.2.1 PCC Scenario

The average Reynolds number and average temperature of the gas flowing from the core into the upper plenum is shown in Figures 17 and 18. The calculation was performed using a model that divided the annular core into three rings. Further, because the model was constructed to study the capability of the MHTGR to survive a PCC scenario without the availability of external heat sinks, e.g., a heat exchanger located in the balance-of-plant, natural circulation flow was restricted to the MHTGR vessel.

Figure 17, showing the average Reynolds number behavior, indicates that by approximately 8 hours ($\sim 0.3 \times 10^5$ s) into the transient, the flow has the following characteristics:

- Flow from the rings with highest power (rings 1 and 2) is upward while flow in the peripheral ring is downward.
- The Reynolds number in rings 1 and 2 is less than 200 from 8 hours onward.

These flow characteristics indicate that plumes are already present by 8 hours.

Figure 18 shows the average temperature for the gas moving from rings 1 and 2 into the upper plenum.

The average temperature reaches 900 K in about 3 hours (627 °C) but does not reach peak temperature (950 K = 677 °C) until 2.8 days (2.4×10^5 hours). Although gas temperatures near 700 °C are not so alarming for the VHTR design, one must consider that with an average temperature of 700 °C there is certainly the possibility of some jets or plumes moving from the core into the upper plenum with temperatures 200 °C or even 300 °C higher than the average. And temperatures of these magnitudes may be present within the first 3 hours of the scenario.

The above calculation suggests the following:

- The portion of the PCC scenario where jets are present (as opposed to plumes) should be determined—since jets with temperature in the vicinity of 1000 °C may be present—and such jets may result in damaging thermal gradients in the ceiling of the upper plenum and also the internal structures, e.g., the control rod housings, etc.
- The locus of points which define the presence of jets should be defined and the heat transfer characteristics evaluated.

10.2.2 DCC Scenario

The average Reynolds number and average temperature of the gas flowing from the core into the upper plenum is shown in Figures 19 and 20. The calculation was performed using the same model for the reactor vessel as for the PCC calculation—but the confinement air was allowed to flow into the lower plenum, following the depressurization; and the natural circulation flow moving upward from the core into the upper plenum was allowed to flow down the riser and out the hot duct outer annulus into the confinement. Therefore all three core rings had gas moving upward into the upper plenum. However, the gas in the core moved at very low Reynolds numbers for the DCC scenario as indicated in Figure 19. Thus, even though the gas temperatures were much higher for the DCC scenario than for the PCC scenario, the gas clearly moved into the upper plenum as very slow moving plumes and created stratified gas layers that would result

in uniform heat transfer to the upper plenum structures with a low probability of localized high thermal stresses.

10.2.3 Concluding Remarks on Data Superposition

A comprehensive investigation of the conditions which give jets capable of impinging on the ceiling of the upper plenum structures is needed. The investigation should consist of two components:

1. An experimental component where the experiments are designed to obtain validation data not only to define the jet behavior—especially with respect to the jet average and maximum velocities upon exiting the core but also the evolution of jets to plumes.
2. A calculation component—using a high-fidelity Multiphysics analysis tool such as NEK5000 –validated using the experimental data obtained in item 1 above, to investigate the jet impingement characteristics at temperature for the MHTGR.

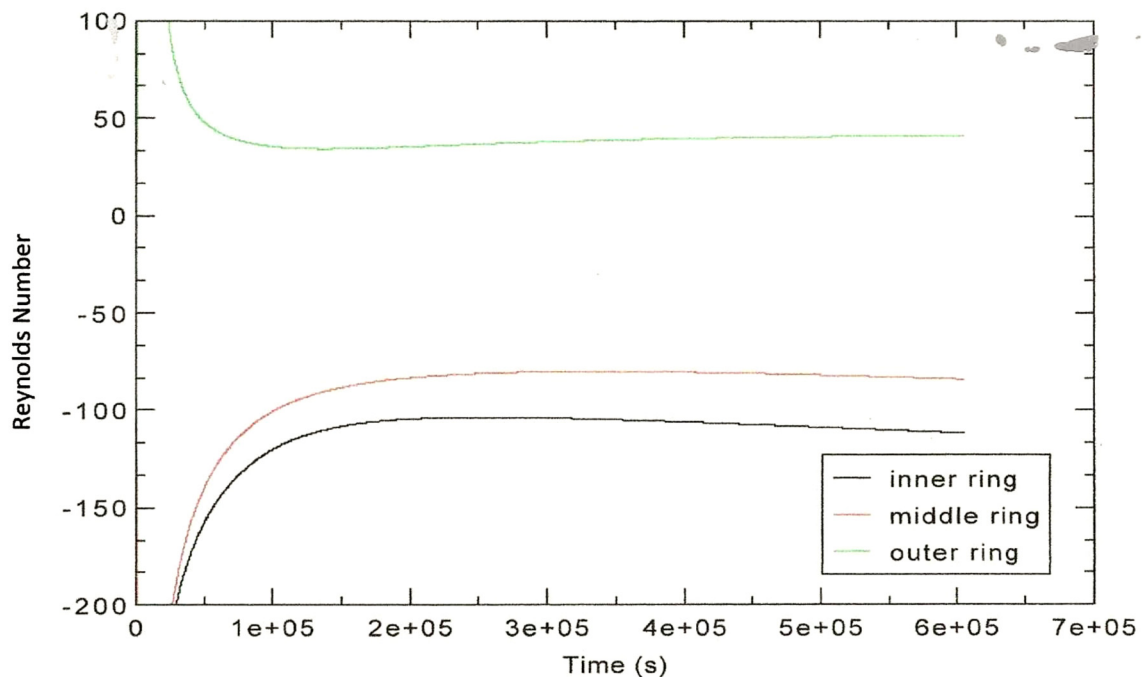


Figure 17: Average Reynolds Number of gases moving from core into upper plenum of MHTGR during PCC scenario from rings 1, 2, and 3

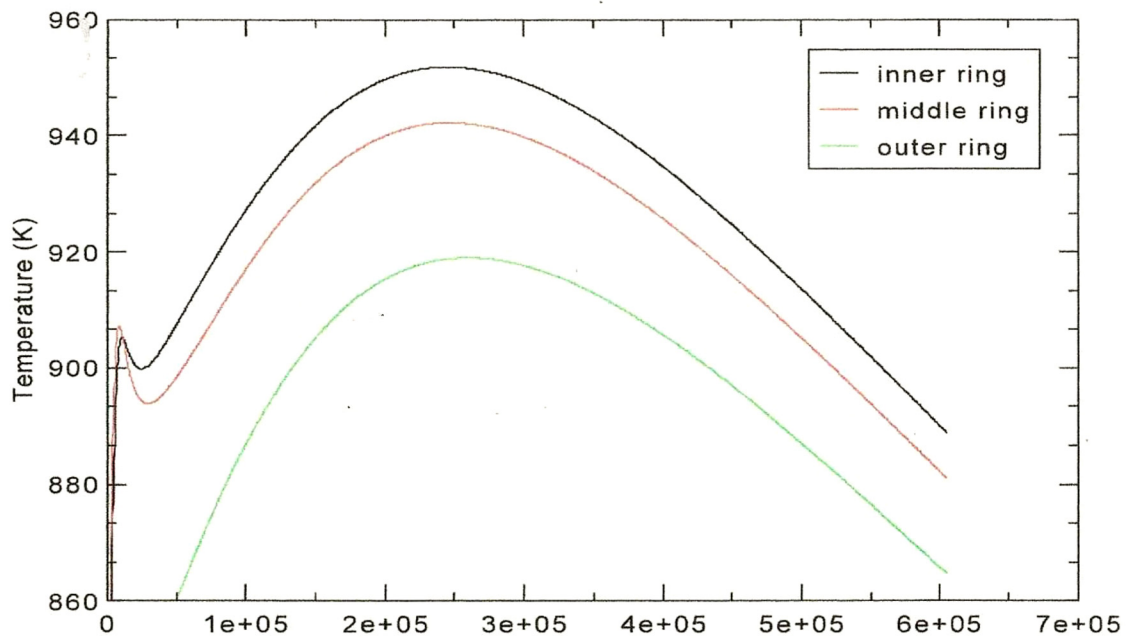


Figure 18: Average temperature of gases moving from core into upper plenum of MHTGR during PCC scenario from rings 1, 2, and 3

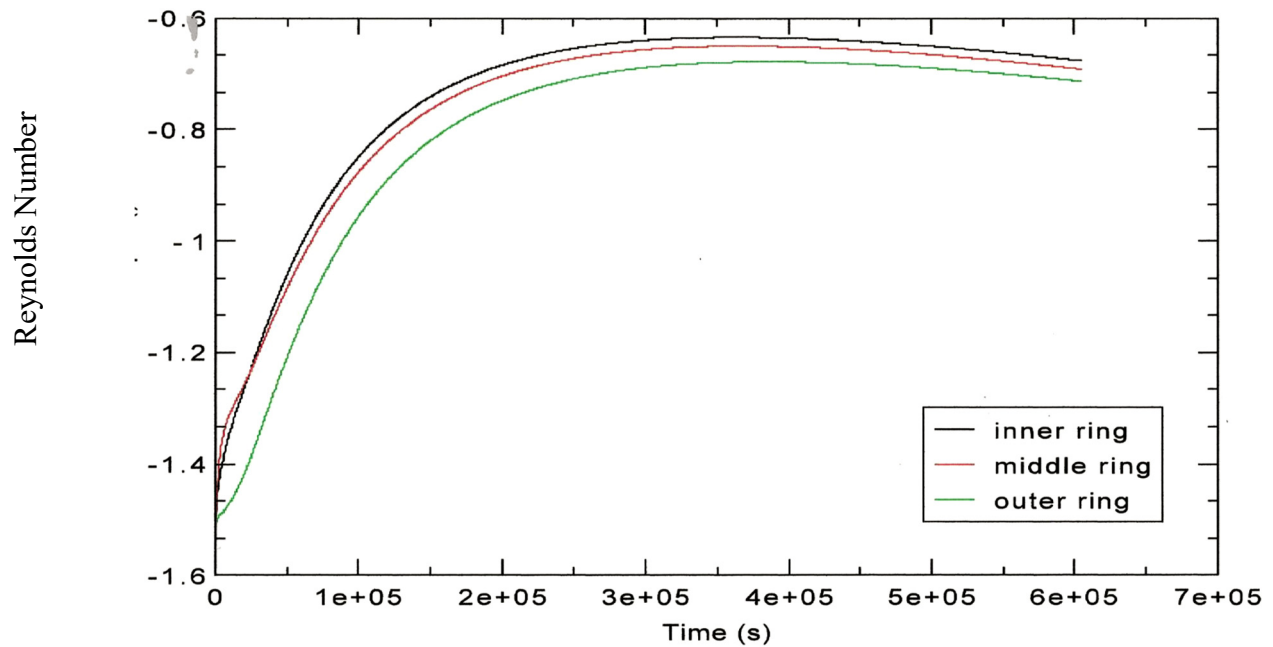


Figure 19: Average Reynolds Number of gases moving from core into upper plenum of MHTGR during DCC scenario from rings 1, 2, and 3

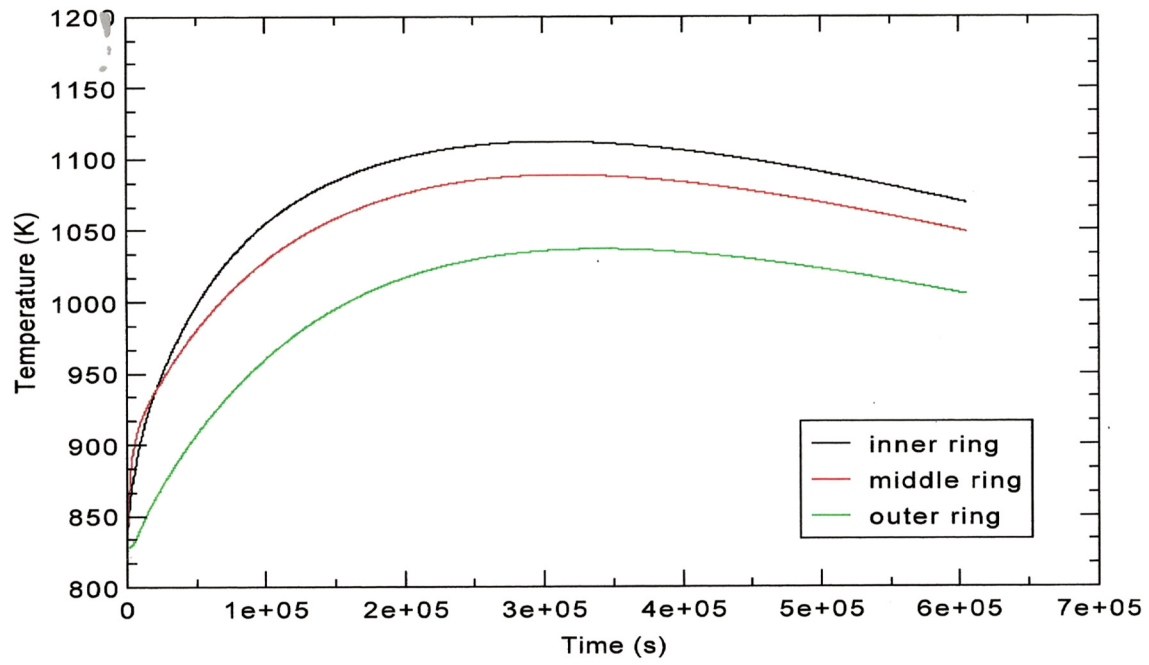


Figure 20: Average Reynolds Number of gases moving from core into upper plenum of MHTGR during DCC scenario from rings 1, 2, and 3

11. Previously Conducted Experiments

A number of fundamental experiments have been performed in the past; some of which can be termed as basic tests as depicted in the validation pyramid (Figure-1). In reality the foundation of the pyramid is made up of validation data from such basic experiments designed to study fundamental phenomena. Data collected from such experiments describes the behavior of the key phenomena in an environment free of extraneous influences, e.g., influences from other phenomena.

11.1 Heated vertical tube ("hot channel" issue)

If buoyancy forces become significant in vertical turbulent flow through a heated duct, the convective heat transfer can become inhibited in upflow while in downflow it could be enhanced; these observations are opposite to those for laminar flow and are not as one might expect [Jackson, Cotton and Axcell, 1989]. With a specified wall heat flux, the Grashof number is usually defined as

$$Gr^* = g\beta q''_{wall} D_h^4 / (k\tau^2)$$

Applying the Dittus-Boelter correlation for gases and the Blasius friction correlation, Jackson developed the following criterion for fully-developed flow in circular tubes:

$$Bo^* = \frac{Gr^*}{Re D_h^{3.425} Pr^{0.8}}$$

As shown in Figure-21, the data of Li [1994] and the semi-empirical model of Jackson and Hall [Jackson, Cotton and Axcell, eqn. 11, 1989] demonstrate that the value of $Bo^* \approx 6 \times 10^{-7}$ provides a reasonable order-of-magnitude estimate of the buoyancy threshold for vertical circular tubes.

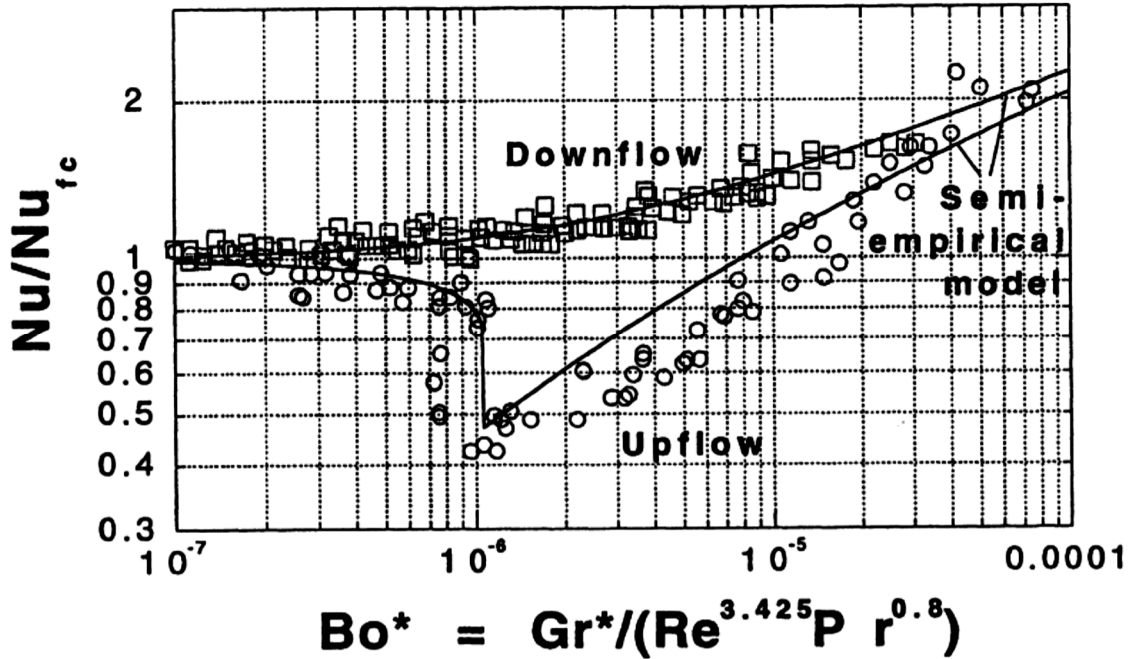


Figure 21: Effects of buoyancy on convective heat transfer for fully-developed flow in vertical circular tubes [Jackson, Cotton and Axcell, 1989; Li, 1994].

Non-dimensionalization of the governing equations for strongly-heated laminar flow in a vertical circular tube, as by Worsoe-Schmidt and Leppert [1965; Worsoe-Schmidt, 1966] yields a different non-dimensional heat flux parameter,

$$Q^+ = r_w q''_{wall}/(kT) = Dq''_{wall}/(2kT)$$

and a buoyancy parameter,

$$(Gr_{ws}/Re) = (gD^3/\tau^2) / (GD/\sigma)$$

based on inlet temperature, plus the property-law exponents. The heat transfer predictions for uniform wall heat flux are shown in Figure-22 in terms of the local Nusselt number and local Graetz number ($= \Phi Re Pr/(4x)$), both evaluated at the local bulk temperature. Flow is from right to left. One sees that for $Q^+ = 5$ and negligible buoyancy there is only a slight influence on Nu and it is constrained to the thermal entry.

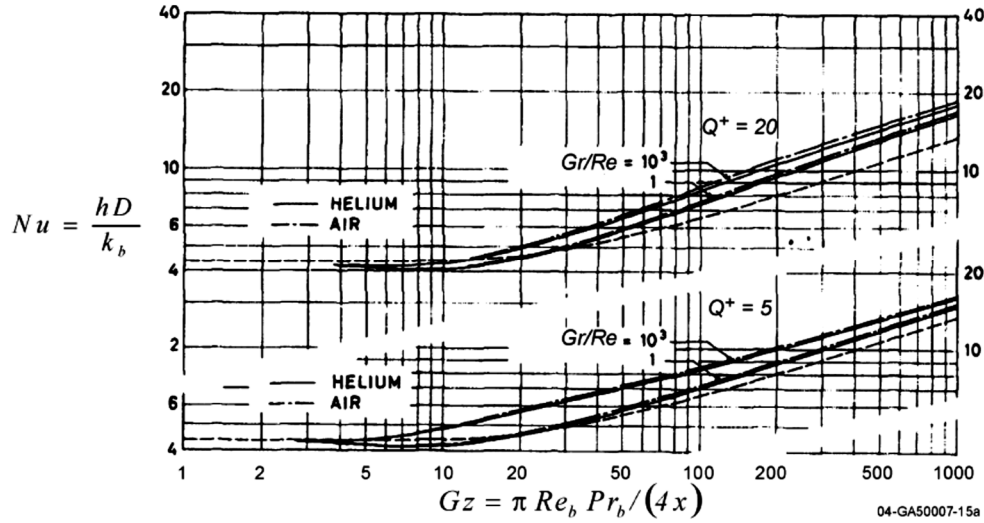


Figure 22: Prediction of local heat transfer parameters for air and helium in laminar flow, accounting for effects of gas property variation [Worsoe-Schmidt, IJHMT 1966].

Some insights into the complicated buoyancy influences were provided by Scheele and Hanratty [1962, 1963]. For well-developed axi-symmetric laminar flow with constant gas properties, several authors [Hallman, 1956; Hanratty, Rosen and Kabel, 1958; Morton, 1960] have derived analytical predictions via the Boussinesq approximation (i.e., density variation only affecting the gravitational body force). Results may be described in terms of the ratio of two dimensionless numbers,

$$G = g \beta q''_{wall} r_w^4 / (k\tau^2) \text{ and}$$

$$R = Re_r = (Vb r_w / \tau) = Re_D / 2$$

for buoyancy and flow rate, respectively where G is the Grashof number. From the definitions, the quantity G/R can be shown to be equivalent to the grouping $Gr_{ws} Q^+ / (4 Re_D)$. Effects on the velocity profiles are shown in Figure-23. In contrast to turbulent flow, an "aiding" laminar flow (heated upflow or cooled downflow) enhances heat transfer parameters; an "opposing" flow reduces these parameters until it becomes unstable and undergoes transition to a turbulent-like flow. In aiding flow the Nusselt number is estimated to be enhanced by about ten per cent when $|G/R|$ is approximately twenty and transition is initiated at $|G/R| \approx 35-40$ or more. For opposing flow, Scheele and Hanratty suggest that at $G/R \approx 9.87$ there is a transition from axi-symmetry to a steady asymmetrical flow with local separation at the wall and then transition to an unsteady and later intermittently turbulent flow begins at about $G/R \approx 52-60$.

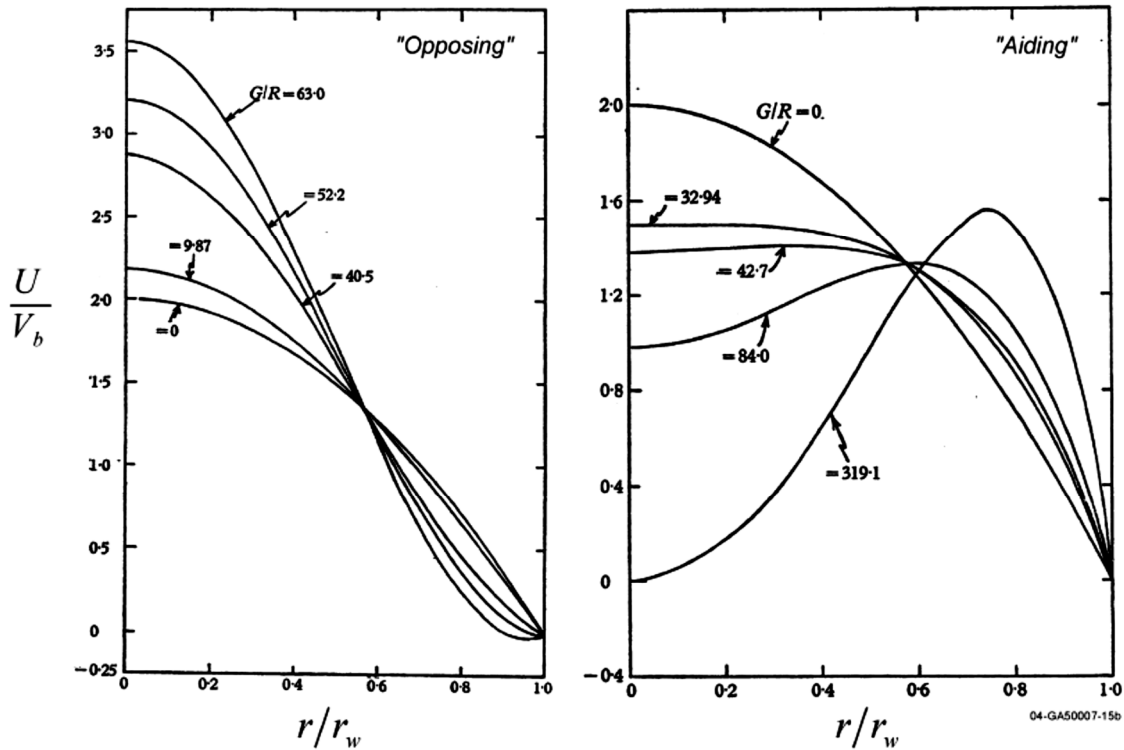


Figure 23: Effects of buoyancy on heated, fully-established laminar flow in vertical circular tubes with the Boussinesq approximation [Scheelee and Hanratty, JFM 1962].

The non-dimensional parameters Re , q^+ , K_v and Bo^* were estimated at the entrance, mid-height and exit of the coolant channels of NGNP for nominal full power and reduced powers of 15% and 10%. The reduced power values were calculated for proportional reductions in gas mass flow rate. These order-of-magnitude estimates are compared to the approximate thresholds for significant effects in Figure-24. Since the viscosity increases with gas temperature, the local Reynolds number decreases along the channels from inlet to outlet. The subfigures in this figure can be considered as "operating conditions maps," comparable to regime maps for a range of experiments.

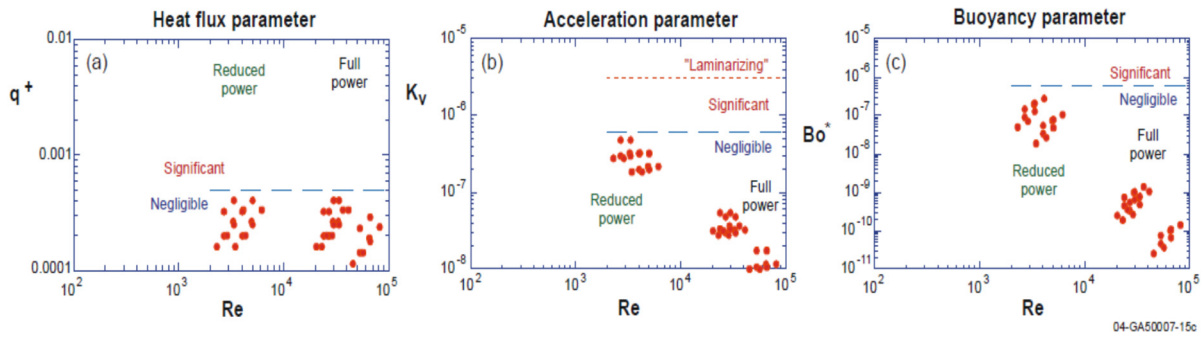


Figure 24: Operating conditions maps for NGNP Point Design during normal full and reduced power operations, order-of-magnitude estimates: a) non-dimensional heat flux (indicator of significance of property variation, b) acceleration parameter and c) buoyancy parameter

Highest gas bulk temperatures occur at the outlet from the active core. The range of outlet Reynolds numbers varied from about 57,000 for a high power core to about 2300 at 10% power. In all cases calculated, q^+ , K_v and Bo^* were low relative to their thresholds for significant effects. A low value of q^+ implies that gas property variation across the channels would have only a slight effect on the local Nusselt number and friction factor. The acceleration parameter K_v provides a measure of the likelihood of laminarization due to streamwise acceleration induced by the reduction in gas density with heating. Likewise, the buoyancy parameter Bo^* indicates whether the heat transfer parameters may be enhanced or reduced as a consequence of buoyancy influences. For the proposed diameters of the coolant channels in the NGNP Point Design, neither property variation, acceleration nor buoyancy would be expected to have significant effects in normal full-power operations.

Data for correlations are available for heated gases over wide ranges of parameters but probably not for all conditions needed, even for circular tubes. Whether all-inclusive correlation equations are possible for system safety codes is doubtful due to the number of possible phenomena to be included. Tabular correlations may be needed.

Mikielewicz et al. [2002] demonstrated that many turbulence models used in general purpose CFD codes fail to predict the simplest case correctly for a circular tube: fully established flow with constant properties (Figure-25). This case should serve as a first test for any turbulence models proposed for heat transfer to the coolant in gas-cooled reactors; in general, models which are inadequate in this situation do poorly at predicting temperatures when fluid properties are varying.

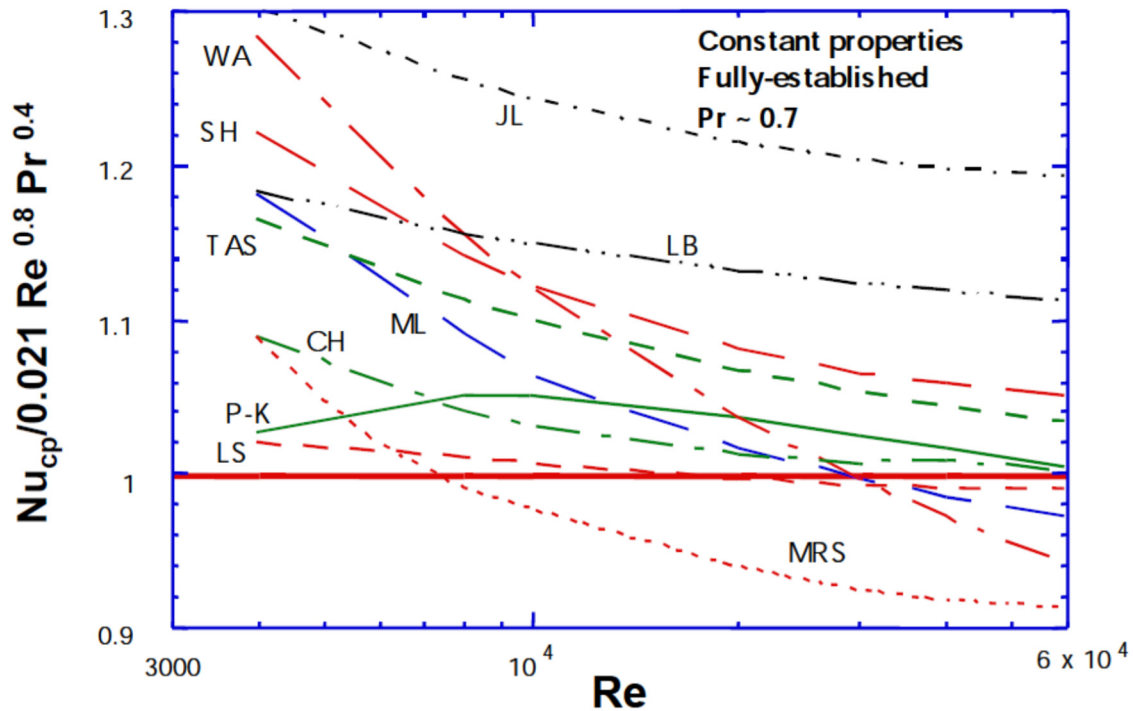


Figure 25: Low-Reynolds-number predictions for fully-established flow in a circular tube with constant properties from various turbulence models [Mikielewicz et al., 2002], normalized by Dittus-Boelter correlation [1930]. Curve labeled P-K is an accepted empirical

1.

To assess correlations of integral heat transfer and friction parameters and for preliminary assessment of turbulence models (Figures-25 and 26), measurements of wall temperatures and pressure drops suffice. Turbulence modelers desire data on internal distributions of turbulence quantities for their models; in general, these quantities have not been measured well with significant gas property variation. There are some careful measurements of internal mean temperature and streamwise velocity distributions which can be used for further intermediate assessment. In either case, to be useful, benchmark data need to be available in tabular form and their conditions and estimated experimental uncertainties [Kline and McIntock, 1953] need to be known. To date, the authors have found such data in the experiments; the ranges of these data are depicted in Figure-26 as regime maps for Re , q^+ and Bo^* .

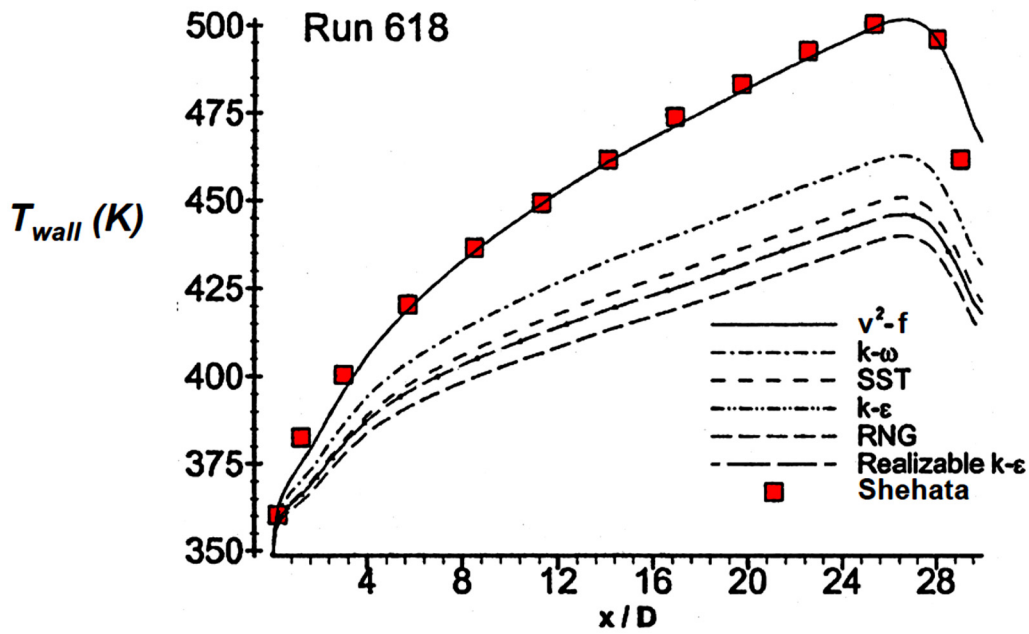


Figure 26: Preliminary assessment of turbulence models via wall temperature data of Shehata [Shehata and McEligot, 1998; Richards, Spall and McEligot, 2004]

Most are for dominant forced convection; however, some comparable data are known to exist for mixed convection (e.g., Prof. Jackson and his colleagues) but tabulations are not yet in hand.

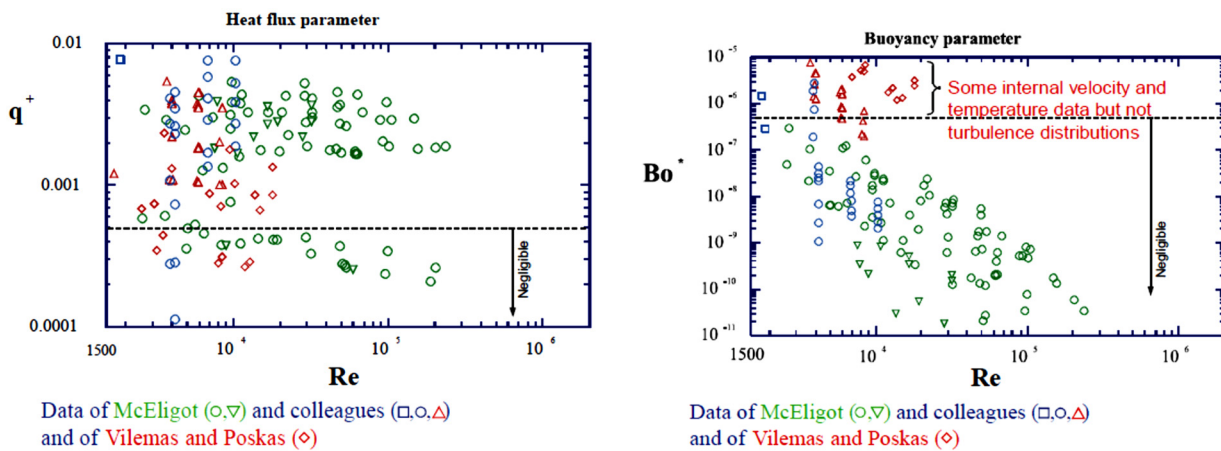


Figure 27: Conditions for which tabulated internal gas heat transfer (and some friction) data are available.

11.2 Lower plenum ("hot streaking" issue)

The flow in the lower plenum can locally be considered to be a situation of multiple buoyant jets into a confined density-stratified crossflow -- with obstructions. Since the flow converges ultimately to a single outlet, the hot jets encounter different crossflow velocities depending on their locations relative to the outlet. The jets furthest from the outlet essentially exhaust into stagnant surroundings between the adjacent posts with the exception of the flow which they induce and some leakage flow. These furthest jets become wall jets (along the corner formed by prismatic outer reflector support blocks) that then impinge on the floor of the plenum. On the other hand, the last row of jets before the outlet encounters crossflow from all the other jets. Figure-28 illustrates this complicated situation via predictions from a CFD model of flow in the lower plenum of a General Atomics GT-MHR reactor [Schultz and Schowalter, 2004]. Further complicating matters are (1) "slot"-type jets from the spaces along the sides of the hexagonal columns in both the reflectors and active core and (2) leakage of cooler gas through the ducts connecting the Shutdown Cooling System Module to the center of the lower plenum.

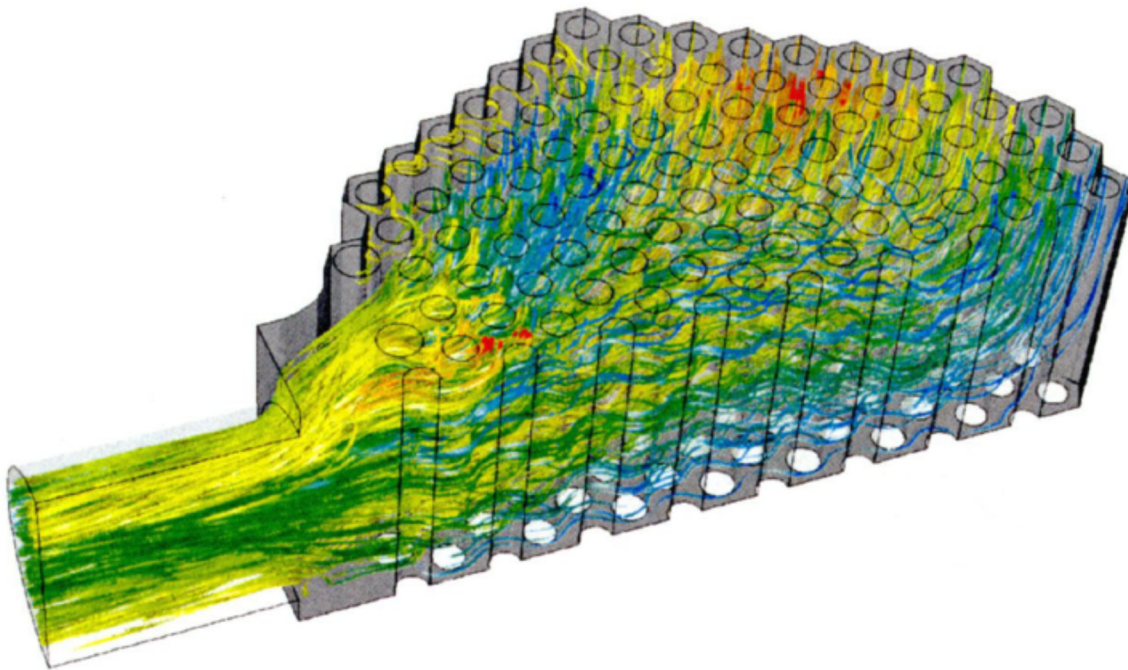


Figure 28: CFD predictions of flow paths and temperatures in a computer model of the lower plenum of a MHTGR (courtesy of General Atomics Co).

11.3 Lower plenum mixing

Possible flow routes in the lower plenum of a typical NGNP concept are demonstrated in plan view in Figure-29. The large circles represent support posts while the smaller ones identify locations of the inlet ducts from the cooling channels in the active core. Some bypass flow can also be expected to enter the lower plenum after passing vertically between the hexagonal graphite blocks both in the core and the reflectors. The arrows give intuitive examples of some paths the flow could be expected to take through the lower plenum from the far side to the outlet duct. In some regions the flow pattern would be comparable to crossflow over a triangular array of rods as in a shell-and-tube heat exchanger; in other locations the flow may tend along passageways formed by parallel rows of posts. The flow rate (or Reynolds number) increases from the right side of the figure to the left as more incoming jets participate.

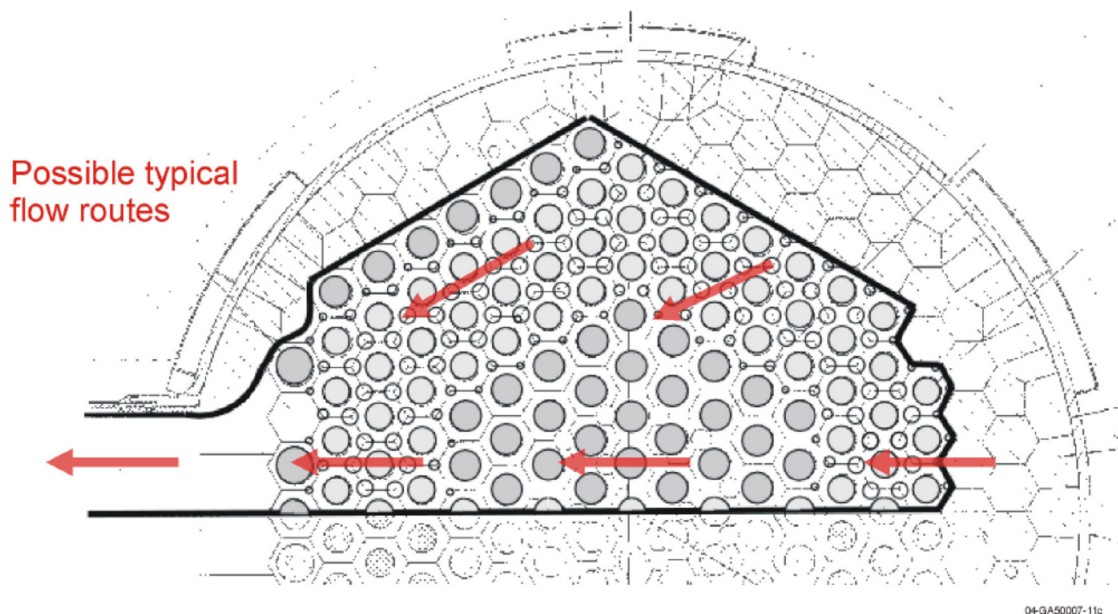


Figure 29: Examples of some possible flow paths in the lower plenum of a typical NGNP concept.

MIR studies are aimed to provide experimental databases for some key coupled phenomena occurring, such as jet interactions with nearby circular posts and with vertical posts in the vicinity of vertical walls - with near stagnant surroundings at one extreme and significant crossflow at the other. As an example, Figure-30 demonstrates a conceptual design for an overall experimental model to be mounted in the test section of the MIR flow system. Pointwise velocities and turbulence components would be determined in three directions by use of our

LDV system; our particle tracking velocimetry (PTV) system might be employed to measure the mixing of particles (representing thermal mixing) from the various jets emanating from simulated reactor cooling channels. Simulated plenum dimensions will be based on geometrical scaling of a current NGNP concept.

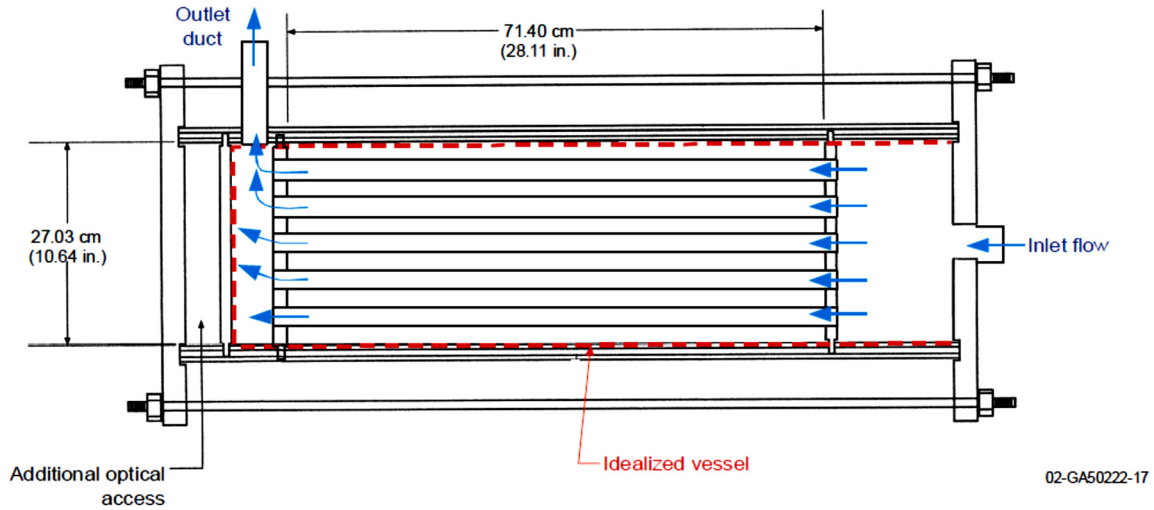


Figure 30: Schematic diagram of conceptual design of MIR experiment model to study mixing, turbulence and flow fields in the lower plenum of an NGNP

12. Summary

Scaling experimental systems play an important role in the validation process. Full-scaled facilities can't be tested under the very detrimental conditions which must be considered when licensing a plant. Most scenarios are examined using scaled facilities and full-scale tests are only performed for adverse conditions for selected components, e.g., a portion of the core. Numerical models must be validated to demonstrate that all key phenomena, including the various interactions between phenomena, can be correctly calculated for the scenarios of interest. This is accomplished using validation data measured in scaled facilities to qualify the numerical models.

During model development and assessment process scaled experiments are used to provide data for the validation matrix/pyramid. The design criteria include the following:

- The scaled experiments must be scaled, using an acceptable methodology, such that the data are in an appropriate range for the plant scenario of interest.
- Must have acceptable measurement uncertainties to provide a reasonable range of acceptance when the data are used to “judge” whether numerical models are capable of calculating the measured phenomena
- Should be designed as a set to create a “validation pyramid” that is comprised of supporting levels:
 - Basic or fundamental experiments give data that describes the behavior of the key phenomena in an environment free of extraneous influences, e.g., influences from other phenomena.
 - Separate effects experiments provide data that describes the behavior of key phenomena in typical system components.
 - Integral effects experiments give data that demonstrates the interactions that occur between the key phenomena for the scenarios of interest.
 - The different scales used in the experiments of the validation pyramid provide a check on the measured experimental phenomena scaling.

The scaling analyses employ both top-down and bottom-up approaches. The top-down scaling approach evaluates the global system behavior and systems interactions from integral test facilities that can be shown to represent the plant-specific design under consideration. The bottom-up scaling analyses address issues raised in the plant- and transient-specific Phenomena Identification Ranking Table (PIRT) related to localized behavior. These analyses are used to explain differences among tests in different experimental facilities and to use these explanations to infer the expected plant behavior and determine whether the experiments provide adequate plant-specific representation.

Scaled facilities based on desired design objective, generate low distribution density vintage data or advanced data with high distribution density. Scaling concepts provide the link between such data measured in integral/separate-effects facilities and the prototype. Theoretically, if scaling distortions are minimized to either a nonintrusive or at least quantifiable level and the scaled experiments are properly scaled, then one can say that if the numerical model can calculate the phenomena measured in the scaled facilities, then the numerical model can also properly represent the phenomena behavior in the prototype for the scenario of the interest.

Argonne National Laboratory has developed NEK5000 advanced multiphysics tool. Both vintage data and advanced data generated from separate effect test facilities and integral facility will be used to validate NEK5000. Once the numerical model is deemed adequate, full-sized prototype plant is then built for analysis.

13. References

(March 2015). “Scaling Analysis for the Very High Temperature Reactor Test Facility at Oregon State University”. OSU-HTTF-OOOOOO-TECH-OOI-R0. B. G. Woods, R. B. Jackson, B. L. Nelson, S. R. Cadell, J. N. Reyes.

(February 2010). “Scaling Studies for High Temperature Test Facility and Modular High Temperature Gas-Cooled Reactor”. INL/EXT-12-24701. Richard R. Schultz, Paul D. Bayless, Brian D. Hawkes, Richard W. Johnson, James R. Wolf, Brian Woods.

(September 2012). “Using CFD to Analyze Nuclear Systems Behavior: Defining the Validation Requirements”. INL/CON-12-27100. Richard R. Schultz.

(2008). “Next Generation Nuclear Plant Licensing Strategy: A Report to Congress, US Nuclear Regulatory Commission and the US Department of Energy”.

(November 2004). “Scaling Studies and Conceptual Experiment Designs for NGNP CFD Assessment”. INEEL/EXT-04-02502. D. M. McEligot and G. E. McCreery.

(2010). “Verification and Validation in Scientific Computing”. William L. Oberkampf and Christopher J. Roy. Cambridge University Press.

(March 2002). “Verification and Validation in Computational Fluid Dynamics”. SAND2002 – 0529. William L. Oberkampf. Timothy G. Trucano.

(December 2005). “Regulatory Guide 1.203”. Office of Nuclear Regulatory Research. U.S. Nuclear Regulatory Commission.

(July 1996). “Gas Turbine-Modular Helium Reactor (GT-MHR) Conceptual Design Report”. Report number 910720/1. General Atomics.

(June 2012). “Natural Circulation Scaling of a Pressurized Conduction Cooldown Event in the Upper Plenum of the Modular High Temperature Gas Reactor”. Thesis submitted to OSU by Brian M. King.

Ball, S. J., et al. (2008). “Next Generation Nuclear Plant Phenomena Identification and Ranking Tables (PIRTs)”. NUREG/CR-6944.

(2012). “Nuclear Systems, Volume 1, Thermal Hydraulic Fundamentals”. Neil E. Todreas, and Mujid S. Kazimi.

(2012) “Computational Fluid Mechanics and Heat Transfer (3rd Edition)”. Richard H. Pletcher, John C. Tannehill, and Dale A. Anderson.

(2010) “Large Matched-Index-of-Refractive (MIR) flow systems for international collaboration in fluid mechanics”. Donald M. McEligot, Stefan Becker, and Hugh M. McIlroy, Jr.